agriculture

MDPI

Article

Hyperspectral Remote Sensing Estimation of Rice Canopy LAI and LCC by UAV Coupled RTM and Machine Learning

Zhongyu Jin [1,2], Hongze Liu [1,2], Huini Cao [1,2], Shilong Li [1,2], Fenghua Yu [1,2,3,*] and Tongyu Xu [1,2,3]

[1] School of Information and Electrical Engineering, Shenyang Agricultural University, Shenyang 110866, China; 2023200006@stu.syau.edu.cn (Z.J.); 2023220016@stu.syau.edu.cn (H.L.); 2023240083@stu.syau.edu.cn (H.C.); 2023220015@stu.syau.edu.cn (S.L.); xutongyu@syau.edu.cn (T.X.)
[2] Key Laboratory of Intelligent Agriculture in Liaoning Province, Shenyang 110866, China
[3] National Digital Agriculture Sub-Center of Innovation (Northeast Region), Shenyang 110866, China
* Correspondence: adan@syau.edu.cn

Abstract: Leaf chlorophyll content (LCC) and leaf area index (LAI) are crucial for rice growth and development, serving as key parameters for assessing nutritional status, growth, water management, and yield prediction. This study introduces a novel canopy radiative transfer model (RTM) by coupling the radiation transfer model for rice leaves (RPIOSL) and unified BRDF model (UBM) models, comparing its simulated canopy hyperspectra with those from the PROSAIL model. Characteristic wavelengths were extracted using Sobol sensitivity analysis and competitive adaptive reweighted sampling methods. Using these wavelengths, rice phenotype estimation models were constructed with back propagation neural network (BPNN), extreme learning machine (ELM), and broad learning system (BLS) methods. The results indicate that the RPIOSL-UBM model's hyperspectra closely match measured data in the 500–650 nm and 750–1000 nm ranges, reducing the root mean square error (RMSE) by 0.0359 compared to the PROSAIL model. The ELM-based models using the RPIOSL-UBM dataset proved most effective for estimating the LAI and LCC, with RMSE values of 0.6357 and 6.0101 $\mu g \cdot cm^{-2}$, respectively. These values show significant improvements over the PROSAIL dataset models, with RMSE reductions of 0.1076 and 6.3297 $\mu g \cdot cm^{-2}$, respectively. The findings demonstrate that the proposed model can effectively estimate rice phenotypic parameters from UAV-measured hyperspectral data, offering a new approach to assess rice nutritional status and enhance cultivation efficiency and yield. This study underscores the potential of advanced modeling techniques in precision agriculture.

Keywords: RPIOSL model; UBM model; LAI; LCC; UAV

Academic Editor: Michael Vohland

Received: 14 November 2024
Revised: 13 December 2024
Accepted: 22 December 2024
Published: 24 December 2024

Citation: Jin, Z.; Liu, H.; Cao, H.; Li, S.; Yu, F.; Xu, T. Hyperspectral Remote Sensing Estimation of Rice Canopy LAI and LCC by UAV Coupled RTM and Machine Learning. *Agriculture* **2025**, *15*, 11. https://doi.org/10.3390/agriculture15010011

1. Introduction

1.1. Importance of LCC and LAI

Leaf chlorophyll content(LCC) and leaf area index (LAI) are vital for rice growth and development, serving as key indicators of the crop's nutritional status [1–3]. Chlorophyll absorbs light energy and converts it into chemical energy to promote photosynthesis and absorbs different wavelengths of light and converts them into energy that can be used by plants [4]. The lack of chlorophyll affects photosynthesis, leading to a decrease in photosynthetic efficiency and affecting plant growth and development [5–7]. The LAI is a measure of the density of the plant leaf area, which reflects the plant's ability to absorb light energy [8], and a higher LAI also helps to regulate the water balance of the plant, while a lower LAI leads to a limitation of photosynthesis, affecting the plant's growth and

development and, then, affecting the yield of rice [9,10]. Therefore, monitoring the LCC and LAI of rice leaves is important for understanding rice growth, water management, and yield prediction, which can help improve the efficiency and yield of rice cultivation [11–13].

1.2. Rationale for Combining Radiative Transfer and Machine Learning Models

Hyperspectral imaging technology is increasingly used in agriculture and has become an important driver of change in modern agriculture [14] . By obtaining spectral information on crops, it is possible to accurately identify crop health, detect pests and diseases, assess nutritional levels, and monitor water content [15–18]. Estimating the phenotypic traits and nutrient elements of rice using hyperspectral data for diagnosing its nutritional status has become a significant research topic for experts and scholars in the field of agricultural information technology, both domestically and internationally [19]. At present, the construction of models to estimate rice phenotypic parameters often adopts a data-driven approach, which is mainly based on machine learning techniques, by constructing a vegetation index or screening characteristic wavelengths [20–22]. Although the data-driven approach is simple and easy to implement, it is affected by multiple factors, such as test locations, varietal differences, and data collection methods, so the generalizability of the model is weak and lacks deep-level mechanistic explanations. In contrast, the crop radiative transfer model (RTM) can emulate the reflectance of the crop canopy by entering phenotypic parameters and explain the association between the spectra and thephenotypic parameters from a mechanistic perspective [23]. Estimating the phenotypic parameters of rice with the help of the RTM can help to make up for the deficiencies of the data-driven approach in terms of mechanism and improve the explanatory power and generalization ability of the estimation model.

1.3. Limitations of Current Methods

The RTM for vegetation leaves simulates the light transmission mechanisms within the foliage, accurately reflecting and transmitting light based on the dynamic changes in various components throughout plant growth [24,25]. The most typical leaf RTM of vegetation is the PROSPECT model, which consists of four phenotypic parameters, that is, structural parameters, chlorophyll, equivalent water thickness, and dry matter weight. Jiang et al. proposed that the layered structure of the leaf blade caused the difference in optical properties and proposed the FASPECT model, in which the upper and lower surfaces of the leaf blade were symmetrically treated as a four-layer structure. Yu et al. [15] adopted the same idea as that of the FASPECT model to construct the FASPECT model. The same idea as in the FASPECT model was used to construct the PIOSL model [26]. Xiang et al. [27] proposed the assumption of layered optical properties of the rice blade structure, combined the PIOSL model based on the assumption of layered optical properties with the structure of the rice blade, and proposed the RPIOSL model capable of simulating the reflectance spectra of rice blades. The model was able to simulate the reflectance spectra of rice leaves with more accuracy by entering the structural parameters of the stratification of the rice leaf, the LCC, the equivalent thickness of water, and the weight of the dry matter. The canopy RTM describes the propagation and interaction of light within the vegetation canopy based on the bidirectional reflectance properties of the vegetation. This model is grounded in the principles of physical optics and takes into account the structure of the vegetation, as well as the processes of light absorption, scattering, and reflection. One of the most well-known canopy RTMs is the SAIL model, which, when combined with the PROSAIL leaf RTM, becomes one of the most commonly used mechanistic models for describing the RT processes in vegetation canopies. However, this model is built on the assumption that the canopy is uniformly distributed, which does not accurately reflect the

condition of rice canopies during the early tillering stage. To address this limitation, Xu et al. [28] developed a vegetation bidirectional reflectance distribution function (BRDF) model based on geometric optics and re-aggregation probability theory, incorporating the structural characteristics of row planting. They optimized the quantitative expression of the optical properties of the canopy in a row structure and provided results for the canopy BRDF model. Since RPIOSL optimizes the internal structure compared with the PROSPECT model, so that the model results are more in line with the measured results of rice leaves, and the UBM breaks the assumption that the vegetation canopy is uniformly distributed compared with the SAIL model, and fully takes into account the structural characteristics of the row structure of the row sown crops, the RPIOSL model coupled with the UBM model was chosen to construct the simulation data set of rice canopy reflectance for the present study. Therefore, in this study, the RPIOSL model coupled with the UBM model was chosen to construct the rice canopy reflectance simulation data set.

Due to the complex non-linear relationship between hyperspectral data and phenotypic covariates, traditional linear regression methods have some limitations in dealing with such problems [29,30]. However, neural networks have powerful nonlinear processing capabilities, and, thus, have been widely used in research related to hyperspectral estimation [31,32]. Luo et al. [33] successfully constructed a model for estimating anthocyanins in peony leaves by using hyperspectral data and employing multiple stepwise regression (MSR), partial least squares (PLS), BPNN, and random forest (RF). In addition, the broad learning system (BLS) proposed by Zhu et al. [34] used ridge regression approximation to compute the pseudo-inverse of the output weights and iteratively updated the pseudo-inverse for regression prediction. Neural networks have the advantage of multiple inputs and multiple outputs and are able to estimate multiple phenotypic covariates at the same time; therefore, in this paper, BPNN, ELM, and BLS neural networks were used for estimation to better deal with the complex nonlinear relationship between hyperspectral data and phenotypic parameters.

1.4. Aim of the Study

Compared to multispectral data and RGB images, hyperspectral data provide richer spectral information [35,36], effectively representing a wide range of plant phenotypic traits [37–39]. However, these data also contain redundancy, as the features of adjacent wavelengths tend to be similar, leading to wasted computational resources and increased model runtime, which limits the application of large-scale phenotypic parameter estimation [40]. Therefore, extracting sensitive wavelengths for chlorophyll and leaf area index (LAI) from hyperspectral data can significantly enhance the efficiency of estimation models. To achieve this goal, this study proposes to employ the competitive adaptive reweighted sampling (CARS) method combined with Sobol sensitivity analysis to extract the sensitive wavelengths for chlorophyll and LAI. The extracted sensitive wavelengths will be used to construct estimation models. The objective of this study is to develop a fast, accurate, and mechanistic estimation model for rice leaf area index (LAI) and leaf chlorophyll content (LCC) by integrating the advantages of data-driven methods with radiative transfer models.

2. Materials and Methods

2.1. Overview of the Study Area and Experimental Design

The study area is located at the Precision Agriculture Aviation Research Base in Gengzhuang Town, Anshan City, Liaoning Province, China (122°43′33″ E, 40°58′43″ N). Gengzhuang Town has flat terrain, fertile soil, and a temperate continental monsoon climate, which is characterized by four distinct seasons, the same rainy and hot seasons,

concentrated precipitation, and abundant sunshine. The temperature difference is large. The average annual precipitation os 652 mm, the average annual temperature is 8.4 °C, the average annual sunshine hours is 3663 h, the annual effective cumulative temperature is 3400 °C–3500 °C, and the mean yearly frost-free duration is 165 d. The rice variety in the test area is Shennong 9816, with a fertility period of about 157 d, which is a medium-late maturing variety. The seedling leaf color is green, the leaf blade is straight, the plant shape is compact, and the tillering capacity is a medium-strong, semi-upright spike type. The experimental area was divided into 11 plots, and the management of all plots was the same, as shown in Figure 1. The experiment was carried out twice in the field at the nodulation and tasseling stages of rice, on 11 July and 15 August 2023, respectively, and representative rice holes were selected to collect canopy spectra, which were analyzed in the laboratory to determine the biochemical parameters. A total of 22 groups of samples were collected in this study, with a digital footprint of 10 GB/ha [41].

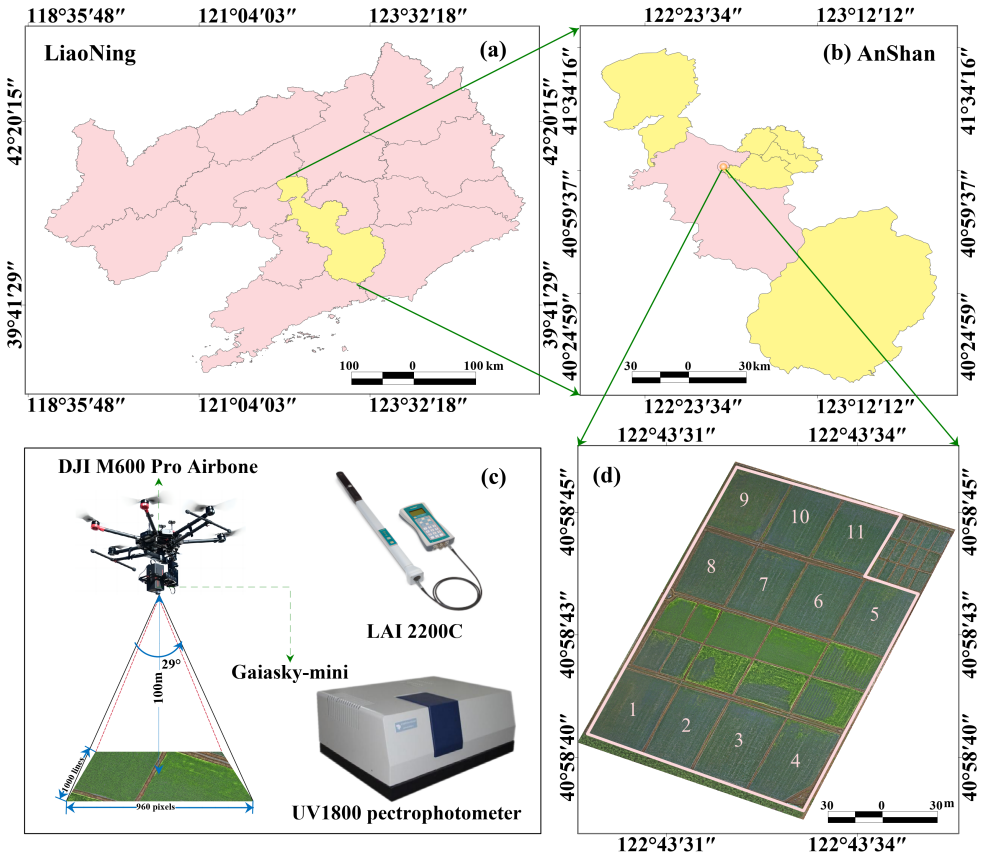

Figure 1. Overview of the study area. (**a**) Vector map of Liaoning Province, with Anshan City in the yellow area; (**b**) vector map of Anshan City, with Gengzhuang Town in the pink area; (**c**) map of instrumentation, including the UAV hyperspectral acquisition system, the LAI 2200C, and the visible-ultraviolet spectrophotometer; and (**d**) map of the experimental area, with the sampling areas labelled 1–11 in the map.

2.2. Data Acquisition

2.2.1. Acquisition of Hyperspectral Data

Canopy hyperspectral acquisition was performed using a UAV-mounted imaging hyperspectrometer (Dualix Spectral Imaging, Wuxi, China). A DJI M600 PRO rotor UAV (DJI-Innovations Inc., Shenzhen, China) was used to carry a built-in GaiaSky-mini push-scan airborne hyperspectral imaging system (Dualix Spectral Imaging, Wuxi, China), which measured the spectral range of 400–1000 nm, with a spectral resolution of 3 nm, a spectral sampling interval of 0.7 nm, and a flight altitude of 100 m. Under clear and cloudless

weather conditions, with good midday light and low wind speeds, it is possible to ensure both stable light and smooth UAV flight. The lens was calibrated with a white board on the ground before measurement, and photos were taken with a standard white cloth for post-collection reflectance calibration after takeoff. After take-off, photos with standard white cloth were taken for post-collection reflectance calibration. The hyperspectral remote sensing data from the UAV platform were collected between 11:00 and 13:00, and during the measurement, the UAV flight speed was set to 2 m/s and the average flight time was 150 min/ha. In the process of data acquisition, the pilot manually controls the UAV hover; the UAV hovered above the test plot and waited for the imaging to complete. Reflectance calibrations and atmospheric corrections were made using the white cloth calibration curve by selecting the captured image with the standard white cloth in the SpectView software (Dualix Spectral Imaging, Wuxi, China). The sampling points were extracted using ENVI5.3+IDL tool software (GeoScene Information Technology Co., Beijing, China), and then, the spectra were resampled and smoothed using Gaussian smoothing method using MATLAB R2023 software with a spectral sample interval of 5 nm after resampling.

2.2.2. Measurement of Sample Data

Data on biophysical and biochemical factors determined in this study included LAI, leaf chlorophyll, equivalent water thickness, and dry matter content. The determination methods were as follows:

- LAI: The LAI was measured using the LAI-2200C canopy analyzer (Li-Cor, Inc., Lincoln, NE, USA), and three LAI values were measured in each graph and then averaged to represent the LAI of the graph; the specific formula is as in Equation (1).

$$LAI = \frac{LAI_1 + LAI_2 + LAI_3}{3}, \quad (1)$$

  Among them, LAI_1 is the first measured LAI, LAI_2 is the second measured LAI, and LAI_3 is the third measured LAI.
- LCC: A rice leaf was sampled, and its maximum length and width were measured to calculate the average leaf area.

$$A_{leaf} = a * b * 0.7746 \quad (2)$$

  where a is the maximum length of leaves, b is the maximum width of leaves, and 0.7746 is the leaf area correction coefficient of rice leaves. A weight of about 0.1 g of fresh rice leaf sample was put into a grinding container, a little quartz sand was added, and the mixture was ground into a homogeneous paste; grinding continued until the tissue became obviously white, and then, it was put on the table to stand. A piece of filter paper was placed in a funnel, the filter paper was moistened with a small amount of ethanol solution, and the extract was slowly injected into the funnel using a glass rod, filtered into a 50 mL volumetric flask. The mantle, the grinding rod, and the glass rod were rinsed with a small amount of ethanol solution, and finally, poured together into a volumetric flask. When it reached the 50 mL mark the volume was fixed at 50 mL by using a rubber burette, and was shaken well. The solution was kept in the dark for up to 24 h (to prevent chlorophyll degradation) until all the chlorophyll had been extracted and a small amount of chlorophyll extract was taken up with a rubber burette and dropped into a colorimetric cup of 1 cm diameter. As blank solution, 95% ethanol was taken and the absorbance of the liquid fraction containing chlorophyll at 665 nm and 649 nm wavelengths was quantified using uv1800pc UV-Vis spectrophotometer (Macylab Instrument Co., Shanghai, China). The concentration

values of chlorophyll *a* and chlorophyll *b* were calculated using Equations (3) and (4) and then converted to μg·cm^{-2} unit [27,42].

$$C_a = 13.95 * \text{A665} - 6.88 * \text{A649} \quad (3)$$

$$C_b = 24.96 * \text{A649} - 7.32 * \text{A665} \quad (4)$$

where A665 indicates the absorbance of the 665 nm sample and A649 indicates the absorbance of the 649 nm sample, C_a is the content of chlorophyll *a*, C_b is the content of chlorophyll *b*, and LCC is equal to the sum of chlorophyll *a* and chlorophyll *b*.

- Equivalent water thickness: A rice leaf was first weighed for its fresh weight M_{fresh}, then, placed in an oven at 105 °C for 30 min, and subsequently, dried at 70 °C until a constant weight was achieved. The dried leaves were reweighed to obtain the dry matter weight M_{dry} and the equivalent water thickness of the leaves was calculated using Equation (5).

$$C_w = \left(M_{dry} - M_{fresh}\right) / A_{leaf} \quad (5)$$

- Dry matter content: Dry matter content was calculated based on the dry matter weight M_{dry} and the average leaf area A_{leaf}.

$$C_m = M_{dry} / A_{leaf} \quad (6)$$

2.3. Methodology

2.3.1. The RPIOSL Model

The RPIOSL model is a sophisticated radiation transfer model tailored for rice leaves, created by refining the parameters of the PIOSL model. Leveraging the Non-dominated Sorting Genetic Algorithm-III (NSGA-III) for parameter optimization, the RPIOSL model precisely simulates the complex processes of light reflection, scattering, and transmission within rice leaves. This model is pivotal in advancing our understanding of the optical properties of rice leaves, thereby enabling the development of highly accurate hyperspectral detection methods for evaluating the physical and chemical parameters of rice. Its application is instrumental in enhancing the monitoring, management, and overall productivity of rice crops, making it a valuable tool for modern agricultural practices.

In this study, both field observations and insights from the existing literature were employed to establish the range of input parameters for the RPIOSL model. These parameters are detailed in Table 1, providing a comprehensive foundation for the model's accurate simulation of light interactions within rice leaves.

Table 1. RPIOSL parameter list.

Parameter	Symbol	Scope	Unit
Structural parameters of the first-layer blade	N_1	1–3	
Structural parameters of the second-layer blade	N_2	1–3	
Leaf chlorophyll content	Cab	0–100	μg·cm^{-2}
Leaf moisture content	Cw	0.004–0.04	μg·cm^{-2}
Leaf dry matter content	Cm	0.0019–0.0165	μg·cm^{-2}
The leaf chlorophyll ratio between the first and second layers	Cab_{12}	0–1	
The leaf water ratio between the first and second layers	Cw_{12}	0–1	
Leaf dry matter ratio between the first and second layers	Cm_{12}	0–1	

2.3.2. Unified BRDF Model for Plants

The Unified BRDF model (UBM) gives an analytical expression of the primary and multiple scattering reflectance for different incident light conditions and vegetation types [28]. Based on geometrical optics, the foothold is shifted from the tree canopy to the vegetation

elements, and the nonisotropic character of the primary scattering term is attributed to the geometrical relationship between the sun-target sensor, the multiscale cluster superposition, and the ratio of the direct sun and sky scattering to the irradiance of the target. As different vegetation types are the result of multiscale cluster superposition, the method of obtaining the four-component area ratio is re-given based on Poisson distribution, so that it is applicable to various vegetation types, and then, an approximate analytical expression for the primary scattering term is obtained. With the help of the theory of "recollision probability", the multiple scattering processes within the canopy and between the canopy and the soil are considered, the formation principle of the multiple scattering term is revealed, and the model parameters are shown in the Table 2.

Table 2. UBM parameter list.

Parameter	Symbol	Scope	Unit
Leaf area index	LAI	1–8	
Zenith angle	θ_i	0–90	◦
Observational angle	θ_v	0–90	◦
Plant height	H	0.1–2.5	m
Gathering index	$Clup$	0–1	
Sky-scattered light ratio	β	0–1	
G function	G	0.5	
Background reflectivity	$background\_reflectance$	0–1	

2.3.3. The PROSAIL Model

The PROSAIL RTM integrates the PROSPECT leaf optical model with the BRDF SAIL model of the vegetation canopy [43], and has been extensively utilized in recent years for estimating vegetation canopy parameters. The PROSPECT model conceptualizes the leaf structure as a multilayered flat plate with rough surfaces. It generates the reflectance and transmittance of leaves across different spectral bands through a sophisticated simulation process that requires the input of various leaf biochemical parameters, such as LCC, dry matter content, equivalent water thickness, and structural parameters.

Conversely, the SAIL model assumes a homogeneous vegetation canopy with leaves exhibiting uniform characteristics in all directions. It is grounded in the theory of RT equations. The reflectance and transmittance outputs from the PROSPECT model serve as inputs for the SAIL model, which then simulates the vegetation structure as a multilayered, rough-surfaced flat plate. This simulation process accurately reproduces the RT phenomena, including multiple reflections and scattering within the vegetation canopy. The parameters used in the model are detailed in Table 3.

Table 3. PROSAIL parameter list.

Parameter	Symbol	Scope	Unit
Leaf structure parameters	N	1–3	
Leaf chlorophyll content	Cab	0–100	$\mu g \cdot cm^{-2}$
Leaf moisture content	Cw	0.004–0.04	$g \cdot cm^{-2}$
Leaf dry matter content	Cm	0.0019–0.0165	$g \cdot cm^{-2}$
Leaf area index	LAI	1–8	
Zenith angle	tts	0–90	◦
Observational angle	tto	0–90	◦
Relative azimuth angle	psi	0–360	◦
Type of leaf inclination angle distribution	$TypeLIDF$	1/2	
Agrotype	$rsoil$	1/2	
Hot parameter	$hspot$	0–1	

2.3.4. Extraction of Hyperspectral Characteristic Wavelengths

Competitive adaptive reweighting sampling (CARS) is a statistical method tailored for variable selection, particularly effective in high-dimensional data analysis such as chemo-

metrics and bioinformatics involving spectral data [44]. The essence of CARS lies in its iterative and adaptive approach to reducing the number of unimportant variables through a competitive process. This enhances both the predictive performance and interpretability of models. CARS excels in handling high-dimensional datasets by minimizing redundancy and noise, thereby improving the accuracy and robustness of predictive models. Its adaptive adjustment and competitive mechanism allow CARS to dynamically customize the variable selection process based on the data's characteristics, resulting in more precise and reliable outcomes.

2.3.5. Machine Learning Methods

- Back propagation neural network: The core advantage of the BPNN algorithm lies in the process of the forward propagation of data and backward propagation of errors, and the use of gradient descent to continually adjust the connection weights and thresholds between neurons in order to bring the results of the network's output layer closer and closer to the desired value. Among many artificial intelligence or neural network algorithms, BPNNs are able to deeply mine, identify, and learn multidimensional nonlinear relationships embedded in massive data. Therefore, with the help of the BPNN's ability to learn intelligently, model highly, and predict accurately in the face of complex multidimensional nonlinear relationships, an attempt can be made to establish an intelligent prediction method, the network structure diagram is shown in Figure 2.

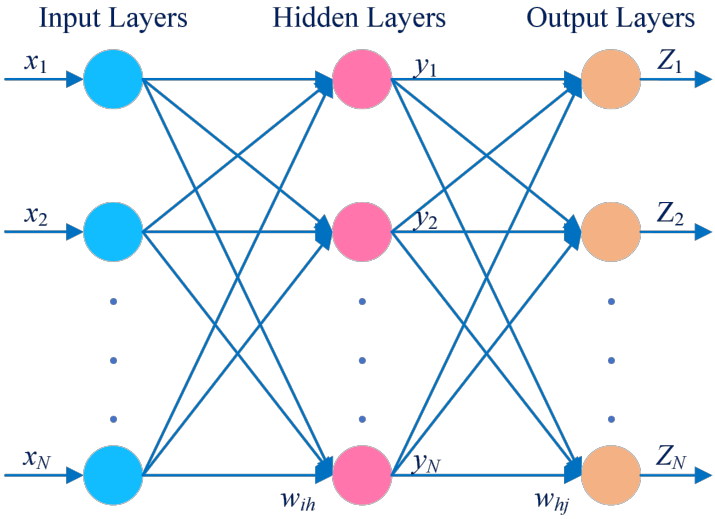

Figure 2. Schematic of BPNN, where blue is the input layer, pink is the implied layer, orange is the output layer, x_1, $x_2 \cdots x_N$ is the input variable, y_1, $y_2 \cdots y_N$ is the intermediate variable, Z_1, $Z_2 \cdots Z_N$ is the output variable, and w_{ih}, w_{hj} is the weight.

- Extreme learning machine: The extreme learning machine (ELM) is an efficient algorithm designed for the rapid training of feedforward neural networks, offering significantly faster learning speeds compared to traditional methods. It operates by randomly generating the weights and biases of the hidden layer and, then, directly computing the output layer weights using the least squares method, thereby greatly simplifying the training process. Unlike traditional neural networks, the ELM does not require iterative optimization, which avoids the local minima issues of gradient descent and significantly accelerates training [45]. Renowned for its speed, simplicity, and robust generalization capabilities, the ELM is widely utilized in a range of machine learning tasks, such as classification, regression, and feature learning, due to its efficiency and rapid training capabilities. Its efficiency in handling large-scale datasets

and real-time applications makes the ELM a highly effective and practical approach to neural network training [46]. The network structure is illustrated in Figure 3.

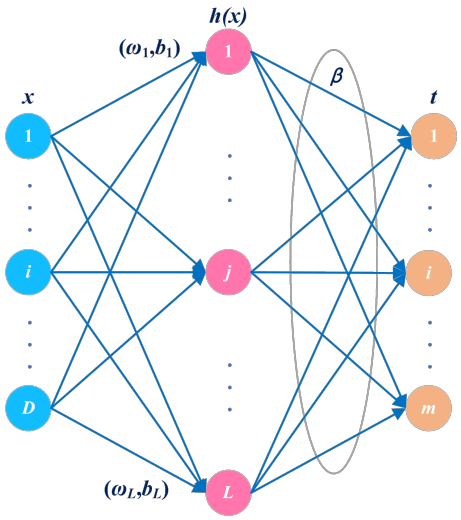

Figure 3. Schematic diagram of the ELM, where blue is the input layer, pink is the hidden layer, orange is the output layer, $1 \cdots D$ is the input variable, $1 \cdots L$ is the intermediate variable, $1 \cdots m$ is the output variable, and ω_L, b_L is the weight.

- Broad learning system: The broad learning system (BLS) is a single-layer incremental learning framework that offers rapid convergence and high accuracy, distinguishing it from traditional deep network models. Its incremental learning capability allows the network model to efficiently scale with growing datasets [34,47]. BLS employs a horizontal scaling strategy, utilizing input-mapped features as the network's feature nodes. These nodes are then expanded into augmentation nodes with randomly generated weights. Both the mapped features and augmentation nodes are directly connected to the outputs, and the corresponding output coefficients are determined using the pseudo-inverse method [48,49]. Therefore, upon the introduction of new neural nodes (including newly incorporated feature nodes), BLS circumvents the necessity for retraining from the ground up. Instead, it merely requires the recalibration of the weights corresponding to the newly added nodes, facilitating rapid incremental learning. The network structure is depicted in Figure 4.

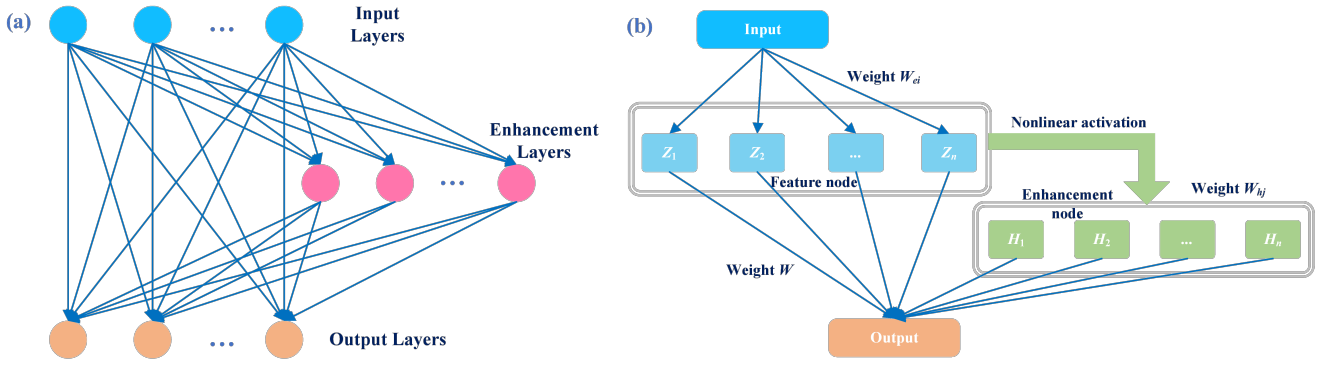

Figure 4. Schematic diagram of BLS. (**a**) Schematic diagram of a neural network connected by traditional random vector functions, where blue is the input layer, pink is the enhancement node, and orange is the output layer; and (**b**) schematic diagram of BLS, including the input layer, feature nodes, enhancement nodes, and the output layer.

2.3.6. Construction of the Model

In this study, 50,000 sets of parameters corresponding to the model were randomly generated based on the measured ranges of physical and chemical parameters based on the PROSAIL model and the RPIOSL-UBM model, respectively. Based on the measured canopy spectra and physicochemical parameter data, the unknown parameters (e.g., N1, N2, etc.) in the RPIOSL model were optimized using the NSGA-III optimization algorithm, and the specific optimization steps are shown in Figure 5.

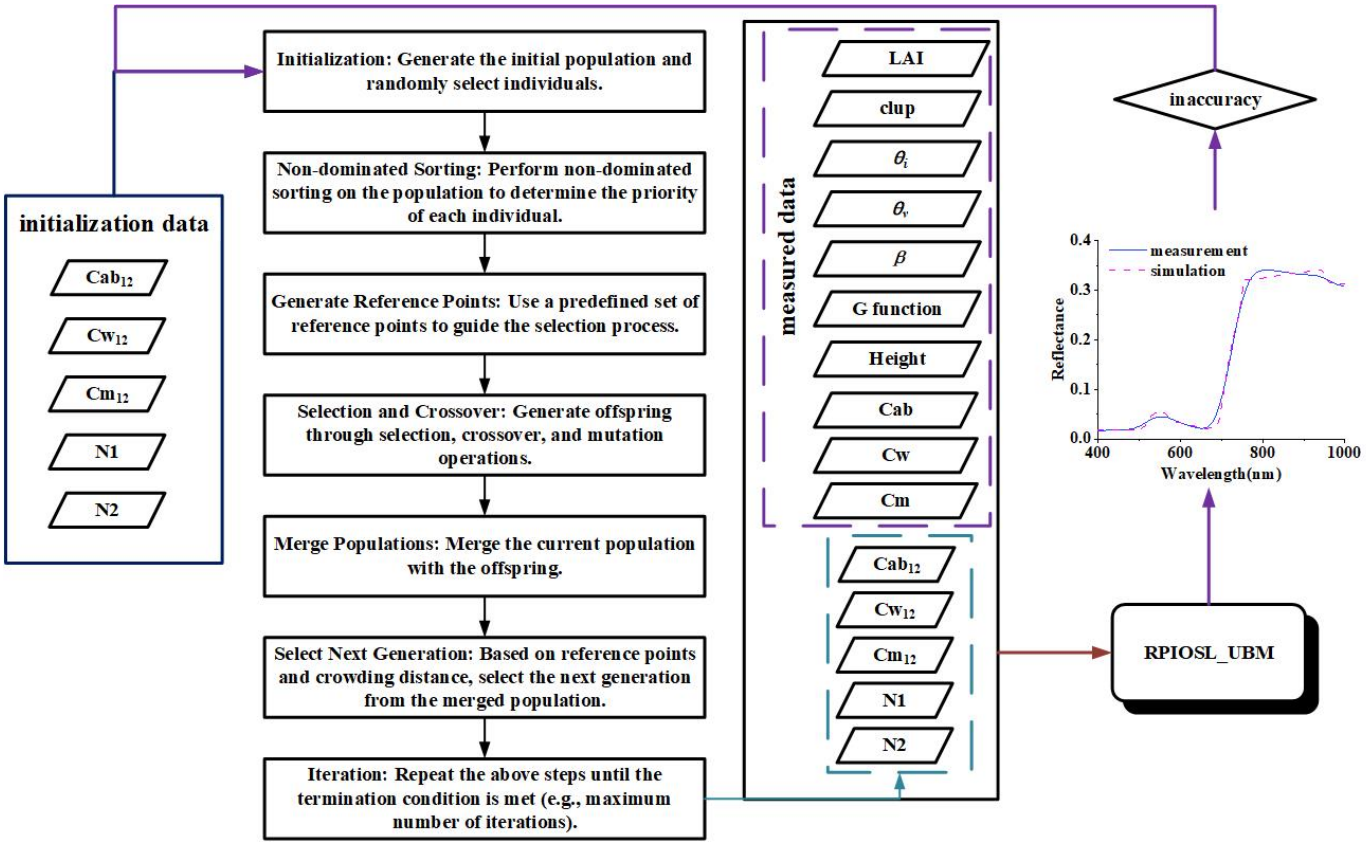

Figure 5. Parameter optimization flowchart. Based on the parameters in the measured data as well as the measured spectral data, the parameters (N1, N2, etc.) were optimized based on the NSGA-III optimization algorithm with the model output spectra and the measured spectral errors as evaluation indexes.

Based on the optimized parameters as well as the measured parameters, the dataset is screened so that the model parameters match the measured data. Sensitivity analyzes of the two RTMs were performed using the Sobol sensitivity analysis method, and the characteristic wavelengths were screened based on the competitive adaptive reweighted sampling method. After the feature wavelengths and parameters screened were randomly divided according to the 7:3 ratio for the training set, the test set, LAI, and LCC were estimated and modeled using the BP neural network, ELM, and BLS, respectively, and precision was verified and evaluated using the measured hyperspectral data from the UAV. Among them, the evaluation indexes of the estimation model are R^2 and RMSE, and the model accuracy validation index is the RMSE of the measured data.The technology roadmap is illustrated in Figure 6.

$$R^2 = 1 - \left(\sum_i (y_i - y_i')^2 / n\right) / \left(\sum_i (y_i - \bar{y})^2 / n\right) \quad (7)$$

$$RMSE = \sqrt{\sum_i (y_i - y_i')^2 / n} \quad (8)$$

where y_i and y_i' represent the measured and simulated values, respectively; $\bar{y}$ is the mean value of measurement; and n is the sample size.

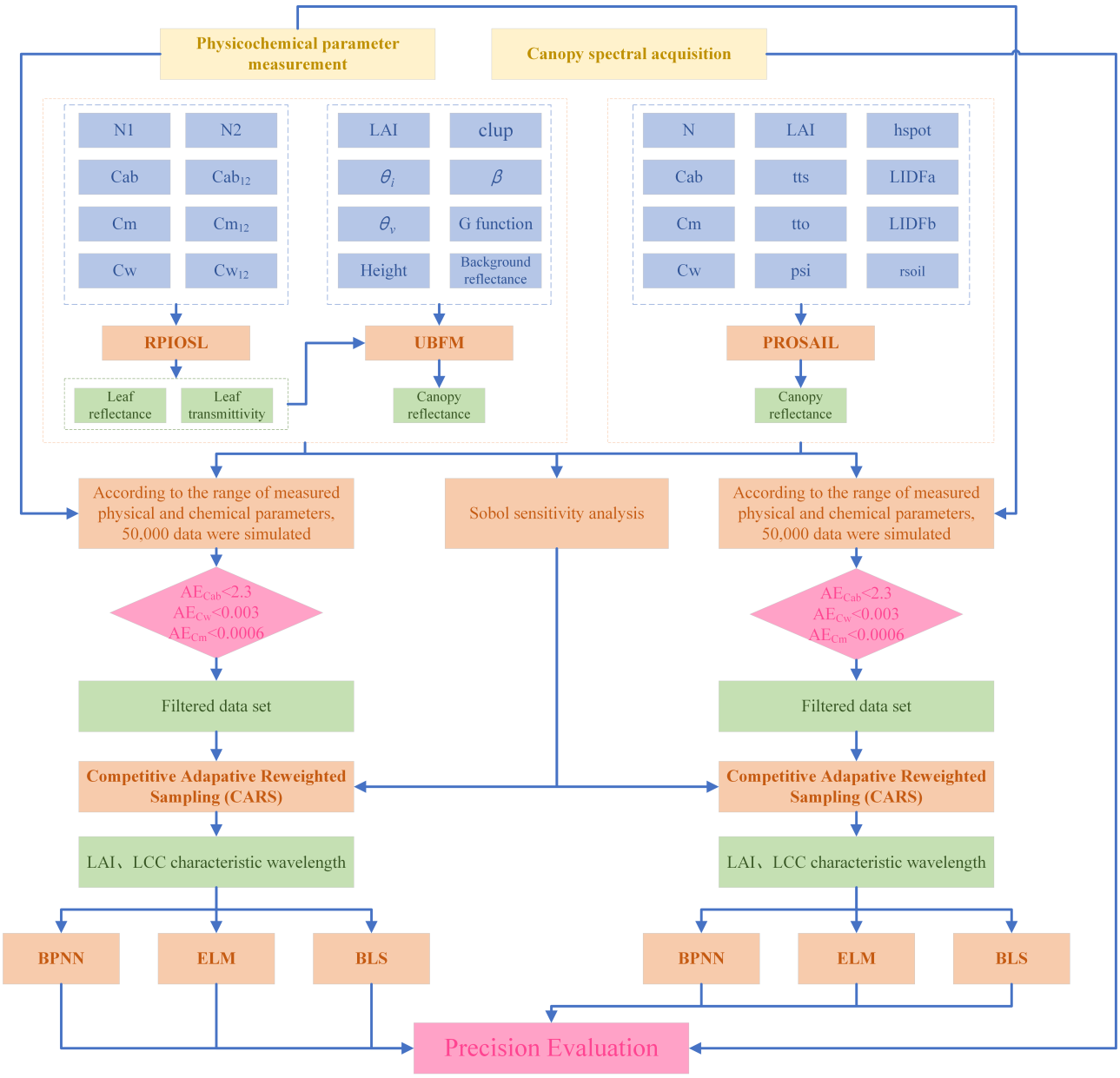

Figure 6. Technical roadmap.

3. Results

3.1. Spectral Simulation Results

In this study, the RPIOSL-UBM model and the PROSAIL model were used to simulate rice canopy spectra, respectively. In both models, the same values were used for the same input parameters (e.g., LAI, LCC, equivalent water thickness, dry matter weight). In addition, the solar zenith angle and observed azimuth angle were also consistent with the measured data. The simulation outcomes are illustrated in Figure 7, and are analyzed in comparison with the measured data. Since the SAIL model is constructed based on the assumption of a uniformly distributed vegetation canopy, the simulation results of the

SAIL model in the near-infrared band range will be biased higher than those of the UBM model and the measured data, as discussed in the analysis in Section 4.1. The RMSE of the model simulation results in the critical band range is shown in Table 4.

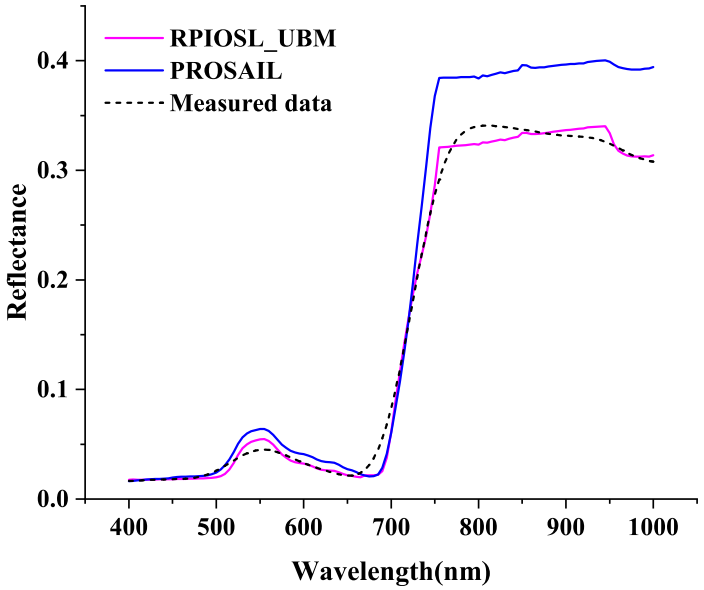

Figure 7. Spectral simulation and sensitivity analysis results.

Table 4. RMSE of model simulation results in the critical band range.

	450–700 nm	800–1000 nm
RPIOSL-UBM	0.0089	0.0082
PROSAIL	0.0115	0.0655

As illustrated in Figure 7 and Table 4, the spectral simulation performance of the RPIOSL-UBM model surpasses that of the PROSAIL model. Notably, the spectra generated by the RPIOSL-UBM model exhibit a closer alignment with the measured spectra. The RMSE of the simulation results in the range of 400–1000 nm for the RPIOSL-UBM model is 0.0086, compared to 0.0446 for the PROSAIL model. This represents a reduction in the RMSE of 0.0359 for the RPIOSL-UBM model, indicating a substantial improvement in simulation accuracy. Moreover, there is a large reduction in the RMSE in both the 450–700 nm and 800–1000 nm band ranges separately.

3.2. Feature-Wavelength Extraction Results

In this study, sensitivity analyses of the two RTMs were conducted independently using the Sobol sensitivity analysis method. The results of these analyses are presented in Figure 8. The sensitivity analyzes were mainly carried out on rice phenotypic covariates, and some of the optically related parameters were not subjected to sensitivity analyses. As depicted in Figure 8a,b, the RPIOSL-UBM model shows that chlorophyll-sensitive bands are primarily located between 400 and 750 nm, while LAI-sensitive bands span the entire range from 400 to 1000 nm, with higher sensitivity observed in the 750–1000 nm range compared to the 400–750 nm range. In contrast, the PROSAIL model indicates that chlorophyll-sensitive bands are mainly confined to the 400–750 nm range, and LAI-sensitive bands are predominantly found in the 750–1000 nm range.

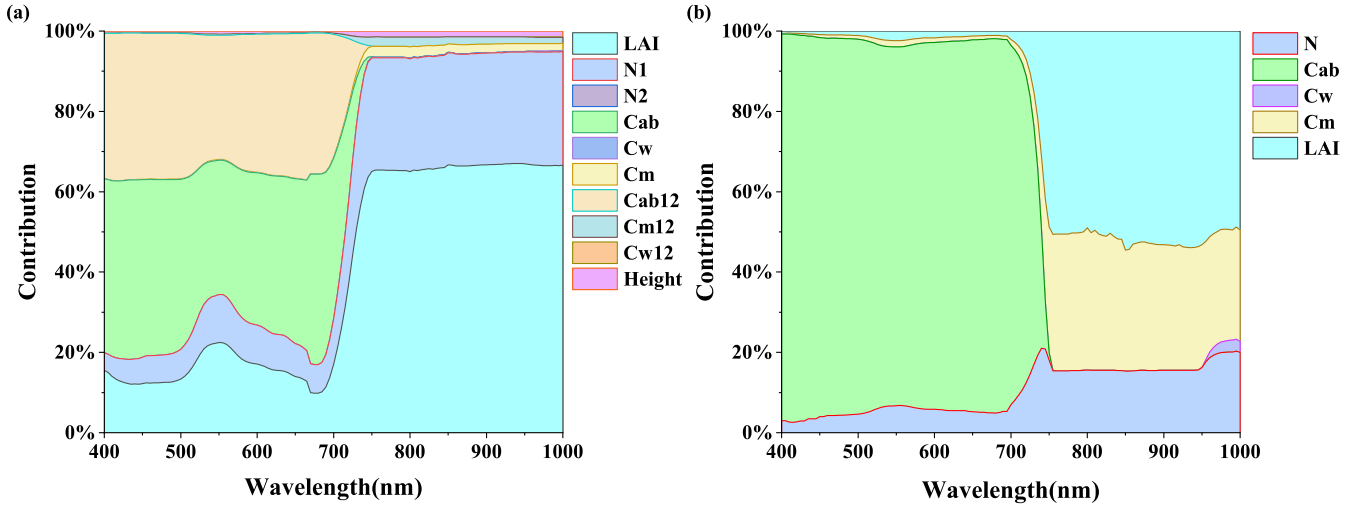

Figure 8. Graph of the sensitivity analysis results, where (**a**) shows the RPIOSL-UBM model sensitivity analysis results and (**b**) shows the PROSAIL model sensitivity analysis results.

In this study, the parameter sets simulated by the two RTMs were screened using measured data, the training and validation datasets were constructed, and the characteristic wavelengths of LAI and LCC were extracted by the competitive adaptive reweighted sampling method, respectively. The LAI and LCC and their corresponding spectral data were subjected to the CARS variable selection process 50 times, respectively, repeatedly selecting the number of generation sampling times and comparing the RMSECV values of each sampling until the optimal subset of variables contained in the smallest RMSECV value was found. The results of feature selection are shown in Figure 9, where 24 chlorophyll feature wavelengths were selected in the RPIOSL-UBM model, namely 415, 430, 435, 440, 445, 465, 470, 480, 530, 535, 540, 575, 580, 585, 590, 620, 680, 780, 820, 830, 860, and 870 nm; 15 LAI characteristic wavelengths were selected, which were 425, 440, 535, 560, 580, 645, 720, 745, 750, 765, 815, 825, 850, 855, and 865 nm. A total of 19 chlorophyll characteristic wavelengths were screened in the PROSAIL model, which were 400, 410, 415, 430, 435, 440, 445, 450, 475, 485, 490, 500, 510, 560, 615, 650, 665, 695, and 700 nm; and 13 LAI characteristic wavelengths were screened as 765, 770, 775, 790, 800, 860, 865, 870, 880, 915, 920, 940, and 945 nm. In the PROSAIL model, the results after feature wavelength extraction using CARS are consistent with the sensitivity analysis results. However, in the RPIOSL-UBM model, the extracted chlorophyll characteristic wavelengths contained wavelengths between 750 and 1000 nm, which was inconsistent with the sensitivity analysis results. Therefore, in this study, the 780 nm, 820 nm, 830 nm, 860 nm, and 870 nm data in the RPIOSL-UBM model were removed, and only the characteristic wavelengths in the wavelength range of 400–750 nm were used for modeling.

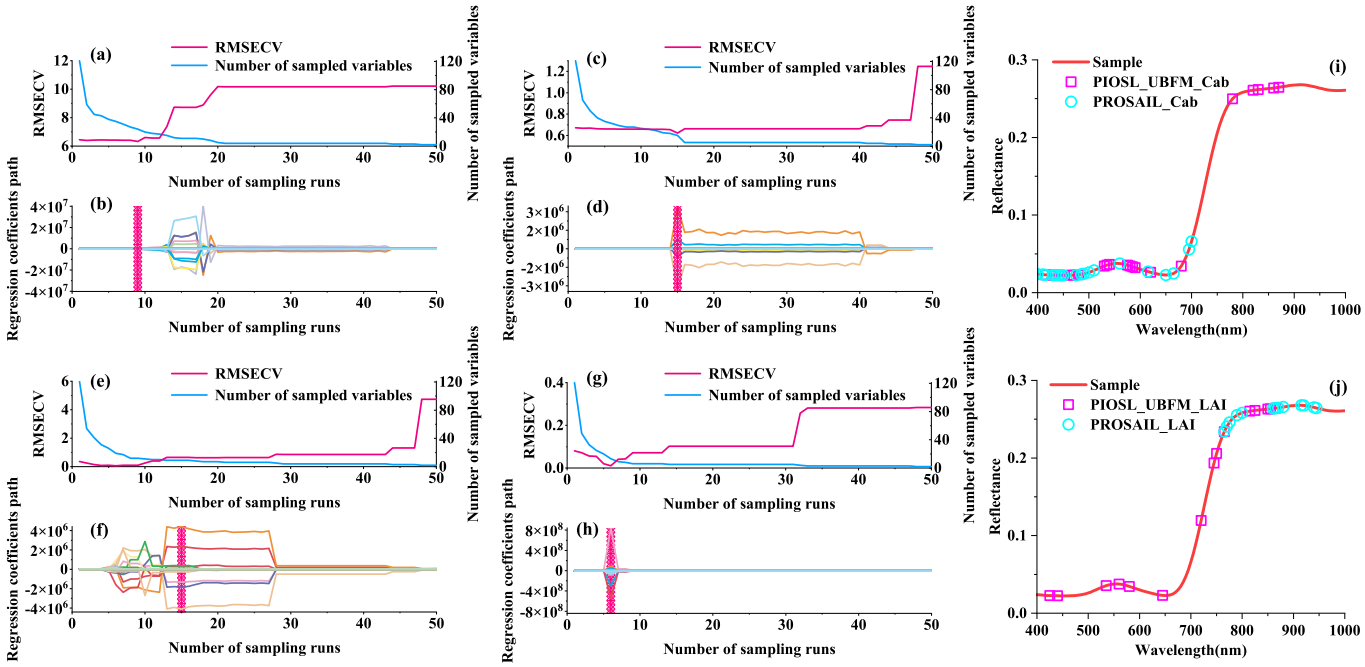

Figure 9. Graphs of feature wavelength screening results, where (**a**,**b**) are the LCC feature wavelength results based on the RPIOSL-UBM model screening; (**c**,**d**) are the LAI feature wavelength results based on the RPIOSL-UBM model screening; (**e**,**f**) are the LCC feature wavelength results based on the PROSAIL model screening; (**g**,**h**) are the PROSAIL model-based screening LAI characteristic wavelength results; (**i**) is a schematic diagram of the LCC characteristic wavelength band of the two RTMs; and (**j**) is a schematic diagram of the LAI characteristic wavelength band of the two RTMs. The pink lines in (**b**,**d**,**f**,**h**) respectively correspond to the minimum RMSECV in (**a**,**c**,**e**,**g**).

3.3. Model Results Based on BPNN Method

To develop a rice phenotypic parameter estimation model for predicting LCC and LAI, a BPNN model was employed. The dataset was divided into training and test sets in a 7:3 ratio and validated using measured data. Due to the differing mechanisms of the two RTMs, the number of neurons required in the hidden layer for the estimation models varied. For the LAI estimation models based on the RPIOSL-UBM and PROSAIL datasets, the number of hidden layer neurons ranged from one to si. For the LCC estimation models, the number of neurons in the hidden layer ranged from 10 to 60 for both datasets. The training results are illustrated in Figure 10, which presents the evaluation metrics. The primary focus of this study is on the validation results using the measured dataset, as the goal is to develop a practically applicable rice phenological parameter estimation model. The graphs reveal that the optimal LAI estimation model, derived from the RPIOSL-UBM dataset, was attained with the incorporation of four hidden layer neurons, yielding an $RMSE_{real}$ of 1.4288. For the PROSAIL dataset, the best LAI estimation model was obtained with one hidden layer neuron, resulting in an $RMSE_{real}$ of 3.5525. Regarding LCC estimation, the optimal model based on the RPIOSL-UBM dataset was achieved with 60 hidden layer neurons, with an $RMSE_{real}$ of 18.08 $\mu g \cdot cm^{-2}$. The best model based on the PROSAIL dataset was obtained with three hidden layer neurons, resulting in an $RMSE_{real}$ of 14.5123 $\mu g \cdot cm^{-2}$. In summary, the BPNN model demonstrated that the LAI estimation model constructed using the RPIOSL-UBM dataset and the LCC estimation model constructed using the PROSAIL dataset performed the best (Table 5).

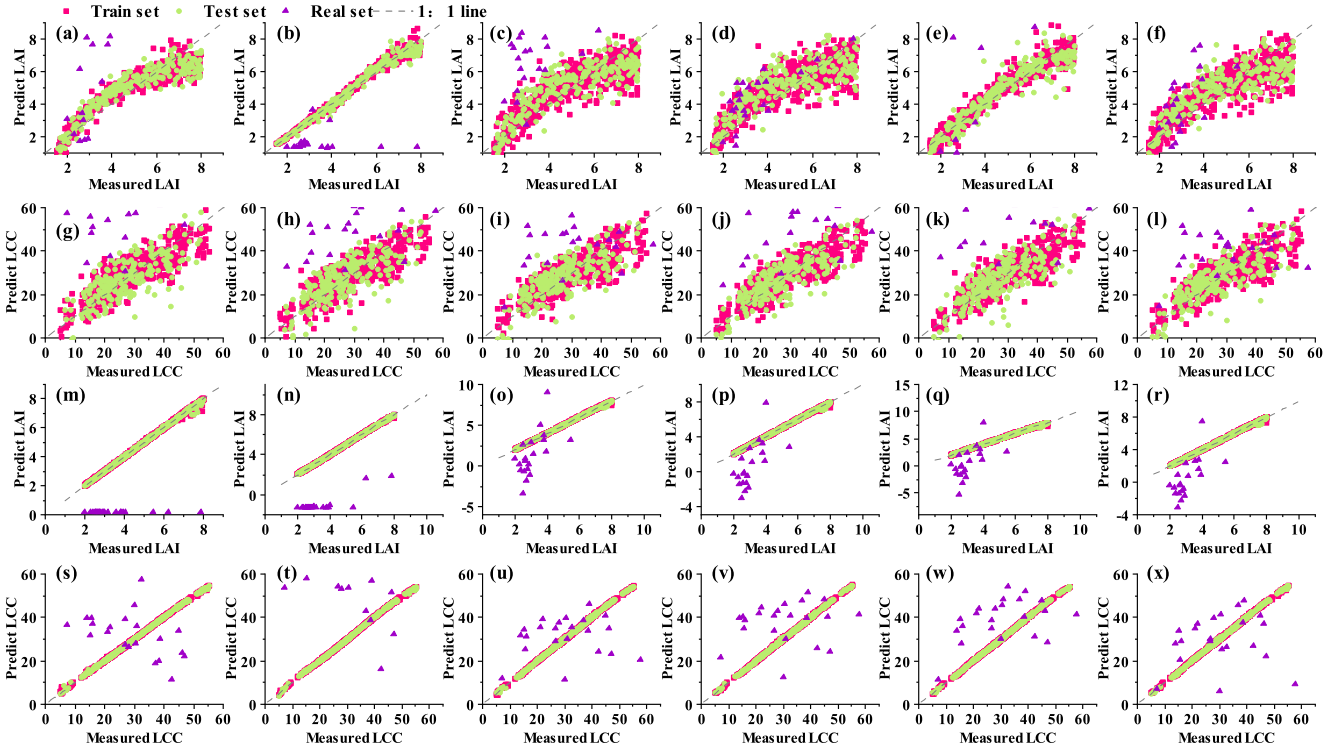

Figure 10. BP neural network-based estimation of LAI and LCC result plots, where (**a**–**f**) are based on the RPIOSL-UBM model to estimate LAI result plots, with the number of implied layers from 1–6, respectively; (**g**–**l**) are based on the RPIOSL-UBM model to estimate LCC result plots, with the number of implied layers from 10–60, respectively; (**m**–**r**) are the result plots of estimated LAI based on the PROSAIL model, with the depth of hidden layers from 1–6, respectively; and (**s**–**x**) are the result plots of estimated LCC based on the PROSAIL model, with the depth of hidden layers from 1–6, respectively.

Table 5. Table of results of estimating LAI and LCC evaluation indexes based on BPNN.

	Model	Evaluation Indicator	1	2	3	4	5	6
LAI	RPIOSL-UBM	Train set R^2	0.8476	0.9864	0.7484	0.7081	0.9354	0.7478
		Test set R^2	0.8106	0.9785	0.6871	0.6401	0.8655	0.6720
		Train set RMSE	0.74	0.2201	0.9460	1.0279	0.4793	0.9468
		Test set RMSE	0.8461	0.2846	1.0847	1.1719	0.7202	1.1067
		Real set RMSE	5.7549	3.9280	3.4980	1.4288	9.0464	2.5146
	PROSAIL	Train set R^2	0.9991	0.9997	0.9997	0.9997	0.9996	0.9996
		Test set R^2	0.9988	0.9997	0.9996	0.9995	0.9995	0.9994
		Train set RMSE	0.0515	0.028	0.0279	0.0313	0.0325	0.0334
		Test set RMSE	0.0593	0.029	0.0317	0.0389	0.0387	0.0408
		Real set RMSE	3.5525	4.5736	6.4012	5.7027	6.0567	6.2243
LCC	RPIOSL-UBM	Train set R^2	0.7228	0.7033	0.6692	0.7135	0.7071	0.6756
		Test set R^2	0.6012	0.6147	0.6036	0.6369	0.6194	0.6258
		Train set RMSE	5.6530	5.8467	6.1743	5.7407	5.8084	6.1070
		Test set RMSE	7.0133	6.6393	6.7994	6.3914	6.6278	6.4353
		Real set RMSE	37.5623	22.9874	19.0587	26.2064	29.0904	18.0800
	PROSAIL	Train set R^2	0.9994	0.9993	0.9993	0.9994	0.9994	0.9993
		Test set R^2	0.9993	0.9992	0.9993	0.9994	0.9994	0.9993
		Train set RMSE	0.2490	0.2631	0.2558	0.2443	0.2435	0.2503
		Test set RMSE	0.2657	0.2896	0.2677	0.2516	0.2582	0.2690
		Real set RMSE	19.7256	54.3931	14.5123	16.1608	14.9091	15.9118

3.4. Model Results Based on ELM Method

To develop a rice phenotypic parameter estimation model for predicting the LCC and LAI, the ELM model was employed. The dataset was partitioned into training and test sets in a 7:3 ratio and validated against empirical data. Due to the differing mechanisms of the two RTMs, the number of neurons required in the hidden layer varied. For the LAI and LCC estimation models based on the RPIOSL-UBM dataset, the number of hidden layer neurons ranged from 10 to 60, whereas for the models based on the PROSAIL dataset, the number of neurons ranged from one to five and included 10. The results of the model training, as depicted in Figure 11, indicate that the LAI estimation model utilizing the RPIOSL-UBM dataset achieved optimal performance with 10 neurons in the hidden layer, achieving an $RMSE_{real}$ of 0.6357, while the PROSAIL-based model performed best with two neurons, achieving an $RMSE_{real}$ of 0.7433. Similarly, the LCC estimation model using the RPIOSL-UBM dataset was optimal with 10 neurons, achieving an $RMSE_{real}$ of 6.0101 $\mu g \cdot cm^{-2}$, whereas the PROSAIL-based model was optimal with one neuron, achieving an $RMSE_{real}$ of 12.5478 $\mu g \cdot cm^{-2}$. Overall, the ELM model showed that the estimation models for LAI and LCC constructed using the RPIOSL-UBM dataset were the most effective, outperforming those based on the PROSAIL dataset (Table 6).

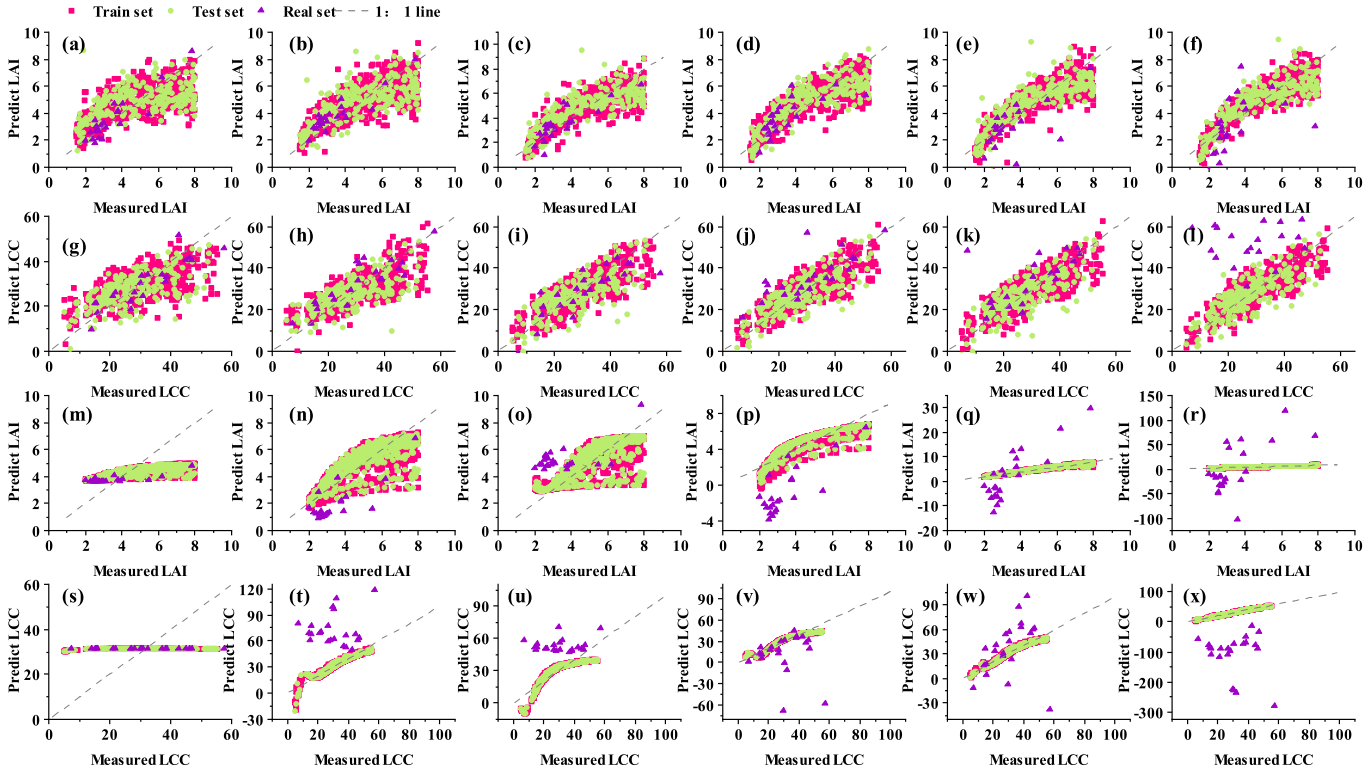

Figure 11. Estimated LAI and LCC result plots based on ELM, where (**a**–**f**) are estimated LAI result plots based on the RPIOSL-UBM model, with the depth of hidden layers from 10–60 respectively; (**g**–**l**) are estimated LCC result plots based on the RPIOSL-UBM model, with the depth of hidden layers from 10–60 respectively; (**m**–**r**) are estimated LCC result plots based on the PROSAIL model estimated LAI result plots, with the depth of hidden layers from 1–5 and 10, respectively; and (**s**–**x**) are estimated LCC result plots based on the PROSAIL model, with the depth of hidden layers from 1–5 and 10, respectively.

Table 6. Table of results of estimating LAI and LCC evaluation indexes based on ELM.

	Model	Evaluation Indicator	1	2	3	4	5	6
LAI	RPIOSL-UBM	Train set R^2	0.4369	0.6088	0.7128	0.7390	0.7776	0.8071
		Test set R^2	0.3373	0.5151	0.6158	0.6622	0.6879	0.7140
		Train set RMSE	1.4139	1.1785	1.0098	0.9627	0.8886	0.8276
		Test set RMSE	1.5739	1.3470	1.2025	1.1272	1.0799	1.0348
		Real set RMSE	0.6357	0.6672	0.7760	0.9928	1.7747	1.9839
	PROSAIL	Train set R^2	0.6612	0.6813	0.7009	0.8065	0.9847	0.9988
		Test set R^2	0.6021	0.6253	0.6545	0.7897	0.9783	0.9984
		Train set RMSE	1.5761	0.9756	0.9453	0.7604	0.2136	0.0603
		Test set RMSE	1.5501	1.0275	0.9891	1.7705	0.2472	0.0677
		Real set RMSE	1.2377	0.7433	2.0863	4.4998	8.9954	48.2324
LCC	RPIOSL-UBM	Train set R^2	0.4044	0.4675	0.6385	0.6603	0.6751	0.7227
		Test set R^2	0.4082	0.3638	0.5715	0.6389	0.6238	0.6542
		Train set RMSE	8.2733	7.8232	6.4453	6.2484	6.1111	5.6448
		Test set RMSE	7.9128	8.2650	6.8419	6.2044	6.5088	6.2459
		Real set RMSE	6.0101	6.1523	7.2157	9.1982	13.9596	29.1397
	PROSAIL	Train set R^2	0.5128	0.7263	0.8922	0.9351	0.9618	0.9973
		Test set R^2	0.5276	0.7372	0.8903	0.9303	0.9627	0.9973
		Train set RMSE	9.7402	5.1313	3.2179	2.4976	1.9157	0.5109
		Test set RMSE	9.9350	5.1196	3.3117	2.6359	1.9289	0.5210
		Real set RMSE	12.5478	26.0820	35.8104	46.3862	31.1645	156.3313

3.5. Model Results Based on BLS Method

In order to build a rice phenotypic parameter estimation model to estimate the LCC and LAI, this subsection was modeled using a BLS framework, with the dataset partitioned into training and test sets at a 7:3 ratio and, subsequently, validated against the measured dataset. Due to the different mechanisms of the two RTMs, the regularization parameters for sparse regularization in building the estimation model are also different. In the LAI and LCC estimation model developed with the RPIOSL-UBM dataset, the regularization parameters were set from 2^{-40} to 2^{-10}. In the LAI and LCC estimation model developed with the PROSAIL dataset, the regularization parameters were configured to span from 2^{-5} to 2^{-10} to 2^{-30}. The outcomes of the model training are illustrated in Figure 12. The evaluation indexes are demonstrated in Table 7. As can be seen in the graphs, the LAI estimation model developed with the RPIOSL-UBM dataset is the most effective when the regularization parameter is 2^{-10} and the $RMSE_{real}$ is 4.5924; the LAI estimation model developed with the PROSAIL dataset is the most effective when the regularization parameter is 2^{-5} and the $RMSE_{real}$ is 4.9139. The LCC estimation model developed with the RPIOSL-UBM dataset is the most effective when the $RMSE_{real}$ is 20.9618 $\mu g \cdot cm^{-2}$; and the LCC estimation model developed with the PROSAIL dataset is the most effective when the $RMSE_{real}$ is 12.3398 $\mu g \cdot cm^{-2}$, when the regularization parameter is 2^{-5}. In conclusion, the BLS model, the LAI estimation model based on RPIOSL-UBFM dataset and the LCC estimation model based on PROSAIL dataset have the best results.

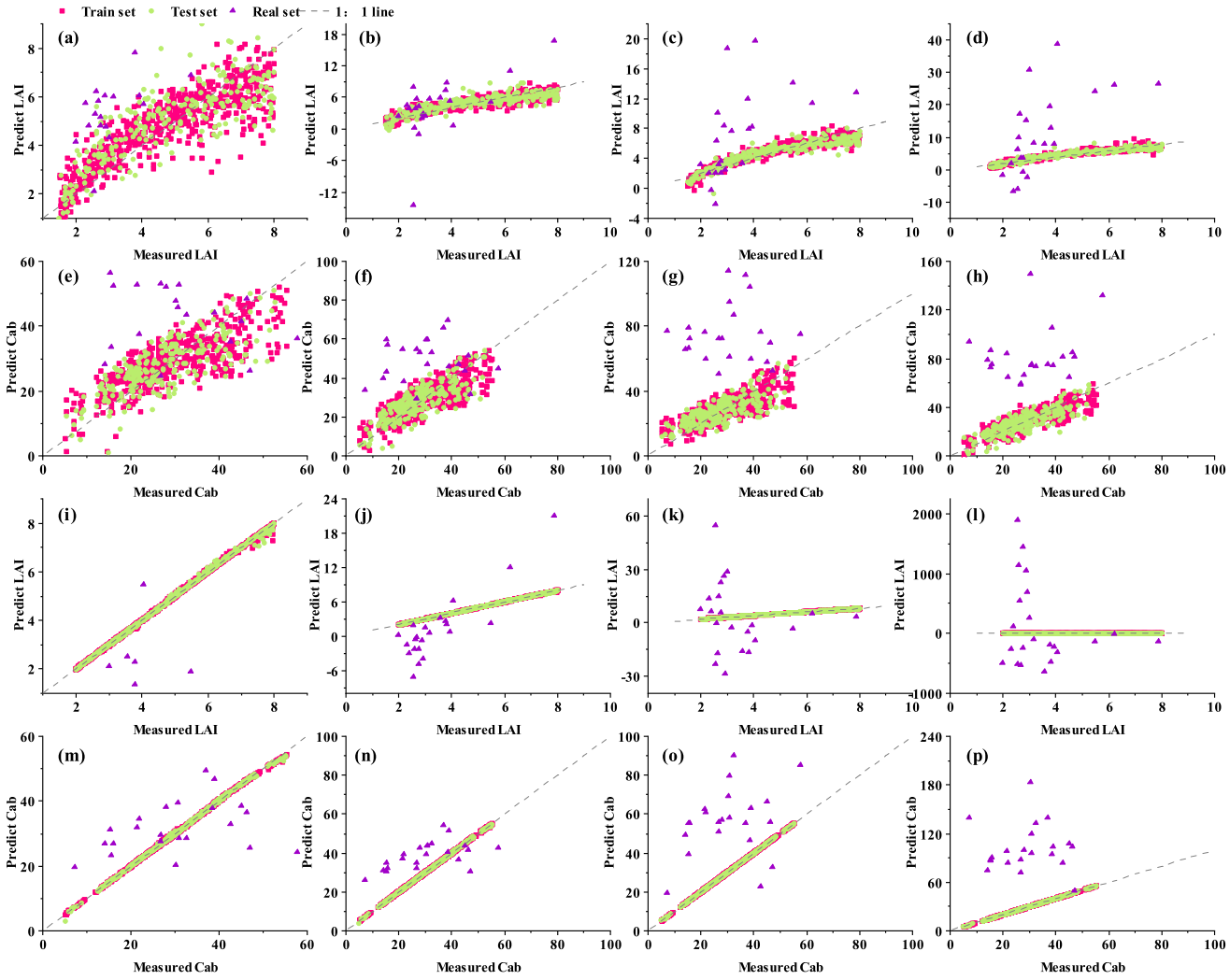

Figure 12. BLS-based estimation of LAI and LCC result plots, where (**a**–**d**) are the LAI result plots based on the RPIOSL-UBM model, with regularization parameters from 2^{-10} to 2^{-40}, respectively; (**e**–**h**) are the LCC result plots based on the RPIOSL-UBM model, with regularization parameters from 2^{-10} to 2^{-40}, respectively; (**i**–**l**) are the LAI result plots based on the PROSAIL model to estimate LAI resultant plots, with regularization parameters from 2^{-5} to 2^{-10} to 2^{-30}; and (**m**–**p**) are PROSAIL model based to estimate LCC resultant plots, with regularization parameters from 2^{-10} to 2^{-40}, respectively.

Table 7. Table of results of estimating LAI and LCC evaluation indexes based on BLS.

	Model	Evaluation Indicator	1	2	3	4
LAI	RPIOSL-UBM	Train set R^2	0.7448	0.8294	0.8697	0.8922
		Test set R^2	0.6449	0.7127	0.8223	0.8777
		Train set RMSE	0.9539	0.7789	0.6830	0.6186
		Test set RMSE	1.1550	1.0377	0.8176	0.6796
		Real set RMSE	4.5924	4.8772	6.2856	13.6650
	PROSAIL	Train set R^2	0.9994	0.9999	0.9997	1.0000
		Test set R^2	0.9990	0.9998	0.9994	1.0000
		Train set RMSE	0.0438	0.0201	0.0293	0.0083
		Test set RMSE	0.0533	0.0266	0.0413	0.0104
		Real set RMSE	4.9139	5.098	19.1130	69.1963

Table 7. *Cont.*

	Model	Evaluation Indicator	1	2	3	4
LCC	RPIOSL-UBM	Train set R^2	0.6193	0.6523	0.5987	0.7067
		Test set R^2	0.6026	0.6676	0.5885	0.7019
		Train set RMSE	6.6385	6.3224	6.7917	5.8070
		Test set RMSE	6.4649	5.9309	6.5804	5.6870
		Real set RMSE	20.9618	24.4485	49.3468	56.2261
	PROSAIL	Train set R^2	0.9993	0.9998	1.0000	1.0000
		Test set R^2	0.9991	0.9998	1.0000	1.0000
		Train set RMSE	0.2631	0.1280	0.0488	0.0092
		Test set RMSE	0.2944	0.1506	0.0476	0.0107
		Real set RMSE	12.3398	13.2870	31.0316	95.7500

4. Discussion

4.1. Discussion of the Accuracy of the Spectral Simulation

The RPIOSL model is a leaf RTM developed with the PROSPECT model, combined with the layered optics assumption and improvements to the rice leaf structure. It was shown that the RPIOSL model was better than the PROSPECT model in simulating the reflectance of rice leaf. Canopy reflectance is mainly composed of leaf reflectance and background reflectance, so the accuracy of the canopy RTM depends not only on the accuracy of leaf reflectance and transmittance but also on whether the simulation mechanism of the canopy RTM is reasonable [50,51]. In this study, the RPIOSL-UBM model, constructed by applying the RPIOSL model coupled with the UBM model, and the PROSAIL model were applied to simulate the hyperspectral reflectance of the rice canopy, respectively, and compared with the measured data. The simulation accuracy of the RPIOSL-UBM model was found to be better than that of the PROSPECT model. In the 500–700 nm band range, the spectra simulated by the RPIOSL-UBM model were closer to the measured data. This is because the RPIOSL model takes into account the actual physiological characteristics of the leaf and the distribution of chlorophyll within the leaf by layering, which makes its simulation better in the visible light range. In the 750–1000 nm band, the spectra simulated by the RPIOSL-UBM model are also closer to the measured data. This is primarily due to the UBM model's more precise consideration of the impact of background reflectance on canopy reflectance. In the SAIL model, only the soil can be selected as wet or dry, and the specific reflectance of the soil cannot be input. On the contrary, rice, unlike dryland crops, spends most of its growing period above a shallow water layer, so it is crucial to input accurate background reflectance in the RTM. Moreover, the SAIL model is based on the assumption of uniform distribution in the canopy, whereas rice, a crop with a ridge structure, is unsealed at the tillering stage and pre-tillering and tasseling stage, and is not uniformly distributed in the canopy, so the simulation results of the SAIL model are not as good as those of the UBM model at the tillering stage and pre-tillering and tasseling stage. The advantage of the coupled canopy radiative transfer model is that it takes into account both the multilayer characteristics of the internal structure of rice leaves and the canopy structure characteristics of rice, a crop with monopoly row structure, thus improving the simulation accuracy. In conclusion, the RPIOSL-UBM model shows higher accuracy in simulating the canopy reflectance of rice by taking the leaf structure, canopy structure, and background reflectance into fine consideration.

4.2. Discussion of Feature Wavelength Extraction

In this study, sensitivity analyses of two canopy RTMs were conducted, revealing that the LCC and LAI exhibited different distributions of sensitivity regions across the two mod-

els. The RPIOSL-UBM model included more physicochemical parameters compared to the PROSAIL model. Since the RPIOSL-UBM model divides the LCC into two layers and introduces the parameter of the stratified proportion of LCC, the contribution of th eLCC was divided into the contribution of LCC and the stratified proportion of LCC in the LCC sensitivity analysis. Overall, the results of the LCC sensitivity analysis in the two models did not differ much. Since the UBM model and the SAIL model are not based on the same evolutionary model, there are differences in the sensitive bands of the LAI in the sensitivity analysis. In this study, hyperspectral reflectance was interpolated to 5 nm intervals in order to improve the running speed of the algorithm, so the results of the characteristic wavelength screening basically do not have the problem of covariance between neighboring wavelengths. The characteristic wavelengths of chlorophyll are predominantly concentrated in the 400–700 nm range, a distribution determined by the light absorption properties of chlorophyll molecules. In this wavelength range, chlorophyll has strong absorption in the blue-violet (430–470 nm) and red (640–660 nm) regions, while it has weak absorption in the green region, which is the reason for the green color of the plant leaves. In the results of the characteristic band screening for LCC, bands within the range of 430–470 nm and 640–660 nm bands appeared, which is consistent with the results of Ban et al. [52] indicating that the characteristic band screening results retained most of the information related to the LCC, and the estimation model of the LCC can be developed with these characteristic band screening results.

The LAI is a critical parameter for quantifying vegetation canopy density and vegetation cover. In the red light band (620–700 nm), chlorophyll absorbs light more strongly, the reflectance of leaves is lower, and the overall reflectance of red light decreases with increasing leaf density, so the reflectance of red light is generally negatively correlated with the LAI [53]. In the near-infrared band (700–1300 nm), the reflectance of leaves is very high due to the strong scattering of near-infrared light by the cellular structure of leaves, and the canopy reflectance increases with an increasing LAI. The red-edge band (680–750 nm) encapsulates the combined effects of chlorophyll absorption and cellular structure scattering. The position and slope of the red edge are highly sensitive to variations in the LAI, making it a crucial band for monitoring the LAI. The reflectance of the green light band (500–570 nm), although less affected by chlorophyll absorption, can still provide some information related to the LAI, which in turn improves the estimation accuracy. Therefore, mechanically speaking, the sensitive band range of the LAI should basically cover the 500–1300 nm band. It is evident that the characteristic wavelength selection results of the RPIOSL-UBM model retain LAI-related information more comprehensively than those of the PROSAIL model.

4.3. Discussion of Model Accuracy Results

In this study, the BPNN, ELM, and BLS methods were used to construct LAI and LCC inversion models, respectively. The specific parameters in the models are shown in Table 8, and the computation times of the training and test sets are shown in Figure 13a and Figure 13b, respectively. Various numbers of hidden layers were utilized to construct the rice phenotypic parameter estimation model based on the BPNN. Analysis of the results indicates that the LCC estimation model, developed using the RPIOSL-UBM dataset, progressively enhanced its validation accuracy on the real dataset as the depth of hidden layers increased. However, the accuracy of the training and validation sets is lower than that of the model with fewer hidden layers. This phenomenon may be attributed to the fact that additional hidden layers enhance the model's ability to capture complex patterns, while simultaneously increasing the risk of overfitting. The LAI estimation model developed with the PROSAIL dataset increases the validation accuracy of the model on the real dataset

as the depth of hidden layers decreases. As can be seen from the subplot of Figure 10m, the model validates better on the real dataset, mainly because the output results are all between 0 and 1, resulting in a lower overall RMSE. However, the results of the model are not distributed around the 1:1 line, indicating that the model is not optimal despite the low RMSE. The LAI estimation model developed with the RPIOSL-UBM dataset showed oscillations in model accuracy, and the R^2 of the training and validation sets did not show a monotonic change with the depth of hidden layers. The model performs better with a medium number of hidden layers. This is because too few hidden layers cannot capture complex patterns, while too many hidden layers tend to lead to overfitting. Therefore, a moderate number of hidden layers strikes a balance between complexity and generalization ability. The LCC estimation model developed with the PROSAIL dataset showed little change in the R^2 and RMSE for the validation and training sets as the depth of hidden layers was changed. Although the results of the validation and training sets look good, the RMSE is larger when validated on the real dataset, and the RMSE of the optimal model for the real dataset is still larger than 14. For LCC estimation, such an error is large and is not suitable to be applied in practical scenarios. In summary, different numbers of hidden layers have different effects on model accuracy. A moderate number of hidden layers can strike a balance between complexity and generalization ability, thus showing better results on the training set, validation set, and real dataset. However, the performance of the model on real datasets needs to be considered comprehensively to ensure the practical application of the model.

Table 8. Model parameter list.

	Static Parameters	Variation Parameters
BPNN	Number of training: 1000; Target error: 0.0001; Learning rate: 0.05.	Number of neurons in the hidden layer: LAI: 1–6; LCC: 10–60.
ELM	Activation function: sig; Regularization factor: 0.	Number of neurons in the hidden layer: RPIOSL-UBM:10–60; PROSAIL: 1–5, 10.
BLS	Shrinkage parameter for enhancement nodes: 0.8; Number of iterations: 200.	Regularization parameter: RPIOSL-UBM: 2^{-10}–2^{-40}; PROSAIL-LAI: 2^{-5}, 2^{-10}–2^{-30}; PROSAIL-LCC: 2^{-10}–2^{-40}.

In developing rice phenotypic parameter estimation models using the ELM, various numbers of hidden layers were employed for analysis. The results indicate that for models estimating the LCC and LAI based on the RPIOSL-UBM dataset, the precision of both the training and validation sets increases with the depth of hidden layers. However, the validation accuracy on the real dataset deteriorates as the depth of hidden layers increases. The best validation performance on the real dataset is observed with the fewest hidden layers, resulting in an RMSE of 0.6357 for LAI estimation and 6.0101 $\mu g \cdot cm^{-2}$ for LCC estimation. At this point, the R^2 values for both the training and validation sets are low, both below 0.5. As the depth of hidden layers increases, the R^2 values for the training and validation sets gradually rise, reflecting the sensitivity of the ELM method to the depth of hidden layers and neuron selection. However, the validation accuracy on the real dataset continues to decrease. Similarly, for LCC and LAI estimation models developed with the PROSAIL dataset, the accuracies of the training and validation sets improve with an increasing number of hidden layers. Nevertheless, the accuracy on the real dataset decreases with more hidden layers. Although the RMSE for both training and validation sets is less than 1 when the depth of hidden layers is 10, the RMSE for the real dataset is

very high, indicating that the model performs well on the training and validation sets but poorly in real-world scenarios. The reason for this is that as the depth of hidden layers increases, the complexity of the model also increases, leading to good performance on the training and validation sets but poor performance on the real dataset. This is a typical overfitting phenomenon, where the model overfits the noise and details in the training data and lacks generalization. The model performs well on the training and validation sets but does not generalize effectively on the real dataset, leading to a decrease in validation accuracy. The ELM has the advantage of fast training but is more sensitive to the number of hidden layers and the choice of neurons. Too many hidden layers may lead to excessive model complexity and increase the risk of overfitting. In summary, although the ELM model performs better on the training and validation sets, the validation accuracy on the real dataset decreases, mainly due to overfitting and dataset differences. By introducing techniques such as regularization, cross-validation, and data enhancement, the effectiveness of the model in real scenarios can be improved.

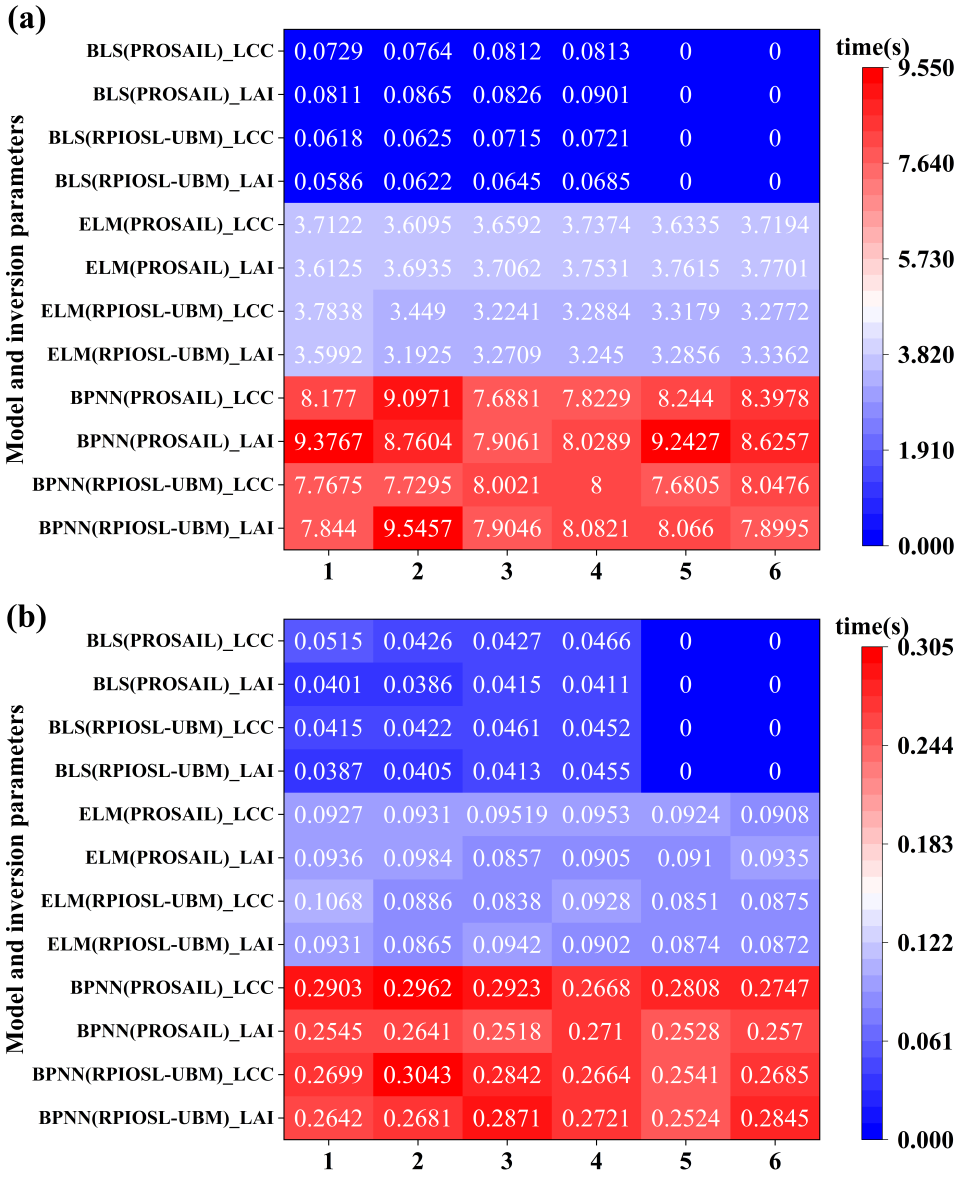

Figure 13. Model runtime graph. Subfigure (**a**) shows the training set runtime heatmap and subfigure (**b**) shows the validation set runtime heatmap, where 1–6 denotes sets 1–6 of parameters.

Different regularization parameters were used for modeling when constructing the rice phenotypic parameter estimation model based on the BLS (broad learning system). The results of the analysis showed that the accuracy of the model in the training and validation sets gradually increased as the regularization parameter was reduced. However, in the model developed with the PROSAIL dataset, the RMSE of the real dataset is very high, despite the R^2 of both training and validation sets being equal to 1, indicating that the model undergoes a serious overfitting phenomenon and has a very poor generalization ability. Furthermore, the RMSE of the LAI and LCC in all models constructed using the BLS method were higher than those constructed using the BP neural network and ELM methods, showing that the BLS method is much inferior to the other two methods in terms of generalizability. The overfitting problem is mainly due to the increase in model complexity caused by the regularization parameter being too small, which makes the model perform well in the training data but poorly on the real dataset. Discrepancies between datasets may also lead to a model performing well on the training and validation sets, yet failing to generalize effectively to the real dataset.

In terms of inversion accuracy, Zhang et al. [54] performed LAI inversion based on RGB and multispectral data, and the results showed that the RMSE ranged from 0.810 to 0.881, whereas the LAI inversion in this study resulted in an RMSE of 0.6357. To analyze the reason for this, this study simulated the effect of LAI changes on the spectra in the range of 700–1000 nm more efficiently by means of the radiative transfer model. In contrast, RGB and multispectral data have less information in the near-infrared band, which leads to a lower accuracy of their inversion. Xu et al. [55] inverted the chlorophyll content of rice leaves based on the PROSAIL radiative transfer model look-up table, and the RMSE of the model was 9.2 $\mu g \cdot cm^{-2}$, while the LCC inversion in this study resulted in an RMSE of 6.0101 $\mu g \cdot cm^{-2}$, which showed a higher accuracy. This enhancement may be attributed to the coupling of the RPIOSL model and the UBM model in this study, which is able to simulate the rice canopy reflectance more accurately compared to the PROSAIL model, thus improving the data accuracy of the look-up table and the inversion accuracy. In summary, further improvement of the simulation accuracy of the radiative transfer model will help to improve the accuracy of the inversion model, which is a direction worthy of in-depth research. The improvement of the model lies not only in the technical innovation, but also in the finer processing of the spectral data, with a view to achieving superior performance in future applications.

In summary, the overfitting phenomenon occurred in both the rice phenotypic parameter estimation models developed with the RPIOSL-UBM dataset and the PROSAIL dataset. The reasons for the overfitting phenomenon can be summarized in two points: First, the models did not select appropriate parameters, such as the quantity of hidden layers and the tuning of regularization parameters; second, there are differences between the model datasets. By observing the construction results of the two RTMs, it can be found that although an overfitting phenomenon exists in both models, the degree of overfitting in the training results based on the RPIOSL-UBM model is better than that of the PROSAIL model, which should be attributed to the fact that the simulation accuracy of the rice canopy hyperspectral spectrum of the RPIOSL-UBM model is better than that of the PROSAIL model. When constructing the model based on the ELM method, setting the number of implied layers to 30 can obtain a more ideal estimation model, and at the same time, the results in the real data validation will not be too bad, and the RMSE is within the acceptable range, which can be applied in the actual production. Therefore, to develop an accurate rice phenotype estimation model based on the RTM, it is imperative to further refine the RTM to ensure that the simulated hyperspectral data closely align with the measured hyperspectral

data; on the other hand, it is necessary to find the appropriate parameters of the model to improve the generalization ability of the model and reduce the risk of overfitting.

4.4. Discussion of Limitations

In this study, an inverse model of LAI and LCC in rice was constructed by coupling leaf and canopy radiative transfer models and based on a machine learning approach. Although the model showed some accuracy in validation, there are still some limitations that need to be further explored. First, in the coupling part of the leaf and canopy radiative transfer models, certain leaf radiative transfer model parameters rely on the results of the optimization algorithm rather than the measured data [27]. This limitation suggests that future research should be devoted to exploring how these parameters can be obtained from measured data to enhance the reliability of the model. In addition, the simulation results of the current radiative transfer model in the 700–1000 nm band still have errors, which may lead to a decrease in the accuracy of LAI inversion. For this reason, future studies should further optimize the canopy radiative transfer model, especially considering the effect of shallow water background on canopy radiative transfer and reflectance when rice is a non-dryland crop. In terms of the inversion model, this study only relied on machine learning, neural network, and wide learning methods to construct the model and did not use optimization algorithms for further optimization. The introduction of optimization algorithms in future studies is expected to improve the model accuracy, thus providing more accurate and reliable data support for field production. In addition, the present model has not been tested in other rice varieties and growing areas, and its generalizability still needs to be further verified and discussed. These limitations provide a clear direction for subsequent research with a view to enhancing the application value and promotion potential of the model.

5. Conclusions

In this study, the RPIOSL model and the UBM model were coupled for the first time to construct a canopy RTM. The accuracy of canopy spectral reflectance simulated by the RPIOSL-UBM model was compared with that of the PROSAIL model. Characteristic wavelengths were extracted using the Sobol sensitivity analysis method and the CARS method. A simulated dataset was selected based on measured data, and rice phenotype estimation models were constructed using BP neural networks and ELM and BLS methods.The results demonstrated that the rice LAI and LCC estimation models, constructed using the RPIOSL-UBM dataset and the ELM method, were optimal. The validation RMSE for the measured dataset was 0.6357 for LAI and 6.0101 $\mu g \cdot cm^{-2}$ for LCC, indicating that the model is suitable for estimating rice phenotypic parameters from UAV hyperspectral data. Compared to models using the PROSAIL dataset, the RMSE for the measured dataset improved by 0.1076 for LAI and 6.3297 $\mu g \cdot cm^{-2}$ for LCC. Future research should focus on selecting the appropriate number of hidden layers to prevent overfitting and improve the accuracy of the RTM simulation. Enhancing the simulation accuracy of the RTM will make it more closely aligned with actual data, thereby improving the precision of rice phenotypic parameter estimation models based on the canopy RTM.

Author Contributions: Z.J.: Methodology, Writing—original draft. H.L.: Visualization. H.C.: Data acquisition. S.L.: Supervision. F.Y.: Conceptualization, Writing—review and editing. T.X.: Funding acquisition, Validation. All authors have read and agreed to the published version of the manuscript.

Funding: This research was supported by the Natural Science Foundation of Liaoning Provincial (Grant No. 2023-MSLH-283), the National Science Foundation of China (Grant No. 32201652), and the Liaoning Province 'Xingliao Talent Program' Project (Grant No. XLYC2203005).

Institutional Review Board Statement: Not applicable.

Data Availability Statement: The raw data supporting the conclusions of this article will be made available by the authors on request.

Acknowledgments: We would like to thank the editors and reviewers for their professional advice on this manuscript.

Conflicts of Interest: The authors declare no conflicts of interest.

References

1. Zhang, B.; Gu, L.; Dai, M.; Bao, X.; Sun, Q.; Zhang, M.; Qu, X.; Li, Z.; Zhen, W.; Gu, X. Estimation of grain filling rate of winter wheat using leaf chlorophyll and LAI extracted from UAV images. *Field Crop. Res.* **2024**, *306*, 109198. [CrossRef]
2. Zhai, W.; Li, C.; Cheng, Q.; Ding, F.; Chen, Z. Exploring Multisource Feature Fusion and Stacking Ensemble Learning for Accurate Estimation of Maize Chlorophyll Content Using Unmanned Aerial Vehicle Remote Sensing. *Remote Sens.* **2023**, *15*, 3454. [CrossRef]
3. Li, W.; Li, D.; Liu, S.; Baret, F.; Ma, Z.; He, C.; Warner, T.; Guo, C.; Cheng, T.; Zhu, Y.; et al. RSARE: A physically-based vegetation index for estimating wheat green LAI to mitigate the impact of leaf chlorophyll content and residue-soil background. *ISPRS-J. Photogramm. Remote Sens.* **2023**, *200*, 138–152. [CrossRef]
4. Zhou, J.; Li, F.; Wang, X.; Yin, H.; Zhang, W.; Du, J.; Pu, H. Hyperspectral and Fluorescence Imaging Approaches for Nondestructive Detection of Rice Chlorophyll. *Plants* **2024**, *13*, 1270. [CrossRef] [PubMed]
5. Ma, Y.; Qiu, C.; Zhang, J.; Pan, D.; Zheng, C.; Sun, H.; Feng, H.; Song, X. Potato Leaf Chlorophyll Content Estimation through Radiative Transfer Modeling and Active Learning. *Agronomy* **2023**, *13*, 3071. [CrossRef]
6. Zhang, S.; Tian, J.; Lu, X.; Tian, Q.; He, S.; Lin, Y.; Li, S.; Zheng, W.; Wen, T.; Mu, X.; et al. Monitoring of chlorophyll content in local saltwort species Suaeda salsa under water and salt stress based on the PROSAIL-D model in coastal wetland. *Remote Sens. Environ.* **2024**, *306*, 114117. [CrossRef]
7. Liu, H.; Lei, X.; Liang, H.; Wang, X. Multi-Model Rice Canopy Chlorophyll Content Inversion Based on UAV Hyperspectral Images. *Sustainability* **2023**, *15*, 7038. [CrossRef]
8. Yuan, W.; Meng, Y.; Li, Y.; Ji, Z.; Kong, Q.; Gao, R.; Su, Z. Research on rice leaf area index estimation based on fusion of texture and spectral information. *Comput. Electron. Agric.* **2023**, *211*, 108016. [CrossRef]
9. Castro-Valdecantos, P.; Apolo-Apolo, O.; Perez-Ruiz, M.; Egea, G. Leaf area index estimations by deep learning models using RGB images and data fusion in maize. *Precis. Agric.* **2022**, *23*, 1949–1966. [CrossRef]
10. Wang, Z.; Chen, J.; Raza, M.; Zhang, J.; Tan, X.; Saeed, A.; Ma, J.; Yang, F.; Yang, W. Predicting maize leaf area index by partial least square combined with wavelet transform. *Agron. J.* **2022**, *114*, 2860–2873. [CrossRef]
11. Li, S.; Jin, Z.; Bai, J.; Xiang, S.; Xu, C.; Yu, F. Research on fertilization decision method for rice tillering stage based on the coupling of UAV hyperspectral remote sensing and WOFOST. *Front. Plant Sci.* **2024**, *15*, 1405239. [CrossRef] [PubMed]
12. Dai, S.; Luo, H.; Hu, Y.; Zheng, Q.; Li, H.; Li, M.; Yu, X.; Chen, B. Retrieving leaf area index of rubber plantation in Hainan Island using empirical and neural network models with Landsat images. *J. Appl. Remote Sens.* **2023**, *17*, 014503. [CrossRef]
13. Sun, J.; Ren, Z.; Cui, J.; Luo, T.; Chen, T.; Yang, W.; Song, P. A high-throughput method for accurate extraction of intact rice panicle traits. *Plant Phenomics* **2024**, *6*, 0213. [CrossRef] [PubMed]
14. Yue, J.; Li, T.; Feng, H.; Fu, Y.; Liu, Y.; Tian, J.; Yang, H.; Yang, G. Enhancing field soil moisture content monitoring using laboratory-based soil spectral measurements and radiative transfer models. *Agric. Commun.* **2024**, *2*, 100060. [CrossRef]
15. Yu, F.; Bai, J.; Jin, Z.; Zhang, H.; Yang, J.; Xu, T. Estimating the rice nitrogen nutrition index based on hyperspectral transform technology. *Front. Plant Sci.* **2023**, *14*, 1118098. [CrossRef]
16. Wang, X.; Xu, G.; Feng, Y.; Peng, J.; Gao, Y.; Li, J.; Han, Z.; Luo, Q.; Ren, H.; You, X.; et al. Estimation Model of Rice Aboveground Dry Biomass Based on the Machine Learning and Hyperspectral Characteristic Parameters of the Canopy. *Agronomy* **2023**, *13*, 1940. [CrossRef]
17. Wang, J.; Wu, B.; Kohnen, V.; Lin, D.; Yang, C.; Wang, X.; Qiang, A.; Liu, W.; Kang, J.; Li, H.; et al. Classification of Rice Yield Using UAV-Based Hyperspectral Imagery and Lodging Feature. *Plant Phenomics* **2021**, *2021*, 9765952. [CrossRef]
18. Song, Y.; Cao, S.; Chu, X.; Zhou, Y.; Xu, Y.; Sun, T.; Zhou, G.; Liu, X. Non-destructive detection of moisture and fatty acid content in rice using hyperspectral imaging and chemometrics. *J. Food Compos. Anal.* **2023**, *121*, 105397. [CrossRef]
19. Xu, T.; Wang, F.; Shi, Z.; Miao, Y. Multi-scale monitoring of rice aboveground biomass by combining spectral and textural information from UAV hyperspectral images. *Int. J. Appl. Earth Obs. Geoinf.* **2024**, *127*, 103655. [CrossRef]
20. Wu, G.; Fang, Y.; Jiang, Q.; Cui, M.; Li, N.; Ou, Y.; Diao, Z.; Zhang, B. Early identification of strawberry leaves disease utilizing hyperspectral imaging combing with spectral features, multiple vegetation indices and textural features. *Comput. Electron. Agric.* **2023**, *204*, 107553. [CrossRef]

21. Qiao, L.; Gao, D.; Zhao, R.; Tang, W.; An, L.; Li, M.; Sun, H. Improving estimation of LAI dynamic by fusion of morphological and vegetation indices based on UAV imagery. *Comput. Electron. Agric.* **2022**, *192*, 106603. [CrossRef]
22. Zou, M.; Liu, Y.; Fu, M.; Li, C.; Zhou, Z.; Meng, H.; Xing, E.; Ren, Y. Combining spectral and texture feature of UAV image with plant height to improve LAI estimation of winter wheat at jointing stage. *Front. Plant Sci.* **2024**, *14*, 1272049. [CrossRef] [PubMed]
23. Tang, Z.; Chen, Z.; Gao, Y.; Xue, R.; Geng, Z.; Bu, Q.; Wang, Y.; Chen, X.; Jiang, Y.; Chen, F.; et al. A Strategy for the Acquisition and Analysis of Image-Based Phenome in Rice during the Whole Growth Period. *Plant Phenomics* **2023**, *5*, 0058. [CrossRef] [PubMed]
24. Chen, Q.; Zheng, B.; Chen, T.; Chapman, S. Integrating a crop growth model and radiative transfer model to improve estimation of crop traits based on deep learning. *J. Exp. Bot.* **2022**, *73*, 6558–6574. [CrossRef]
25. Li, X.; Yu, H.; Yu, Y.; Wang, H.; Zhang, L.; Zhang, X.; Sui, Y. Inversion Model of Clorophyll Content in Rice Based on a Bonic Optimization Algorithm. *Spectrosc. Spectr. Anal.* **2023**, *43*, 93–99. [CrossRef]
26. Jiang, J.; Comar, A.; Weiss, M.; Baret, F. FASPECT: A model of leaf optical properties accounting for the differences between upper and lower faces. *Remote Sens. Environ.* **2021**, *253*, 112205. [CrossRef]
27. Xiang, S.; Jin, Z.; Li, J.; Yu, F.; Xu, T. RPIOSL: Construction of the radiation transfer model for rice leaves. *Plant Methods* **2024**, *20*, 1. [CrossRef]
28. Xu, X.; Fan, W.; Li, J.; Zhao, P.; Chen, G. A unified model of bidirectional reflectance distribution function for the vegetation canopy. *Sci. China-Earth Sci.* **2017**, *60*, 463–477. [CrossRef]
29. Meng, F.; Li, J.; Zhang, Y.; Qi, S.; Tang, Y. Transforming unmanned pineapple picking with spatio-temporal convolutional neural networks. *Comput. Electron. Agric.* **2023**, *214*, 108298. [CrossRef]
30. Du, R.; Lu, J.; Xiang, Y.; Zhang, F.; Chen, J.; Tang, Z.; Shi, H.; Wang, X.; Li, W. Estimation of winter canola growth parameter from UAV multi-angular spectral-texture information using stacking-based ensemble learning model. *Comput. Electron. Agric.* **2024**, *222*, 109074. [CrossRef]
31. Shao, M.; Nie, C.; Zhang, A.; Shi, L.; Zha, Y.; Xu, H.; Yang, H.; Yu, X.; Bai, Y.; Liu, S.; et al. Quantifying effect of maize tassels on LAI estimation based on multispectral imagery and machine learning methods. *Comput. Electron. Agric.* **2023**, *211*, 108029. [CrossRef]
32. Ji, S.; Gu, C.; Xi, X.; Zhang, Z.; Hong, Q.; Huo, Z.; Zhao, H.; Zhang, R.; Li, B.; Tan, C. Quantitative Monitoring of Leaf Area Index in Rice Based on Hyperspectral Feature Bands and Ridge Regression Algorithm. *Remote Sens.* **2022**, *14*, 2777. [CrossRef]
33. Luo, L.; Chang, Q.; Gao, Y.; Jiang, D.; Li, F. Combining Different Transformations of Ground Hyperspectral Data with Unmanned Aerial Vehicle (UAV) Images for Anthocyanin Estimation in Tree Peony Leaves. *Remote Sens.* **2022**, *14*, 2271. [CrossRef]
34. Zhu, H.; Liu, Z.; Chen, C.; Liang, Y. An Efficient Algorithm for the Incremental Broad Learning System by Inverse Cholesky Factorization of a Partitioned Matrix. *IEEE Access* **2021**, *9*, 19294–19303. [CrossRef]
35. Qiu, C.; Ding, F.; He, X.; Wang, M. Apply Physical System Model and Computer Algorithm to Identify Osmanthus Fragrans Seed Vigor Based on Hyperspectral Imaging and Convolutional Neural Network. *Inf. Technol. Control* **2023**, *52*, 887–897. [CrossRef]
36. Wenjing, G.; Xue, C.; Xiaohan, L.; Yusheng, H.; Zhenhui, R. Apple firmness detection method based on hyperspectral technology. *Food Control* **2024**, *166*, 110690. [CrossRef]
37. Li, X.; Wei, Z.; Peng, F.; Liu, J.; Han, G. Non-destructive prediction and visualization of anthocyanin content in mulberry fruits using hyperspectral imaging. *Front. Plant Sci.* **2023**, *14*, 1137198. [CrossRef]
38. Xiao, Q.; Tang, W.; Zhang, C.; Zhou, L.; Feng, L.; Shen, J.; Yan, T.; Gao, P.; He, Y.; Wu, N. Spectral Preprocessing Combined with Deep Transfer Learning to Evaluate Chlorophyll Content in Cotton Leaves. *Plant Phenomics* **2022**, *2022*, 9813841. [CrossRef]
39. Amanah, H.; Wakholi, C.; Perez, M.; Faqeerzada, M.; Tunny, S.; Masithoh, R.; Choung, M.; Kim, K.; Lee, W.; Cho, B. Near-Infrared Hyperspectral Imaging (NIR-HSI) for Nondestructive Prediction of Anthocyanins Content in Black Rice Seeds. *Appl. Sci.* **2021**, *11*, 4841. [CrossRef]
40. Peanusaha, S.; Pourreza, A.; Kamiya, Y.; Fidelibus, M.; Chakraborty, M. Nitrogen retrieval in grapevine (*Vitis vinifera* L.) leaves by hyperspectral sensing. *Remote Sens. Environ.* **2024**, *302*, 113966. [CrossRef]
41. Huang, Q.; Wang, X.; Gao, Q.; Carraro, A.; Sozzi, M.; Marinello, F. Indicators to Digitization Footprint and How to Get Digitization Footprint (Part 2). *Comput. Electron. Agric.* **2024**, *224*, 109206. [CrossRef]
42. Su, X.; He, J.; Li, W.; Pan, Y.; Li, D.; Yao, X.; Cheng, T.; Zhu, Y.; Cao, W.; Tian, Y. Monitoring Rice Leaf Nitrogen Content Based on the Canopy Structure Effect Corrected With a Novel Model PROSPECT-P. *IEEE Trans. Geosci. Remote Sens.* **2024**, *62*, 4414317. [CrossRef]
43. Li, X.; Sun, Z.; Lu, S.; Omasa, K. PROSPECULAR: A model for simulating multi-angular spectral properties of leaves by coupling PROSPECT with a specular function. *Remote Sens. Environ.* **2023**, *297*, 113754. [CrossRef]
44. Xue, H.; Xu, X.; Yang, Y.; Hu, D.; Niu, G. Rapid and Non-Destructive Prediction of Moisture Content in Maize Seeds Using Hyperspectral Imaging. *Sensors* **2024**, *24*, 1855. [CrossRef]
45. Yuan, X.; Zhang, X.; Zhang, N.; Ma, R.; He, D.; Bao, H.; Sun, W. Hyperspectral Estimation of SPAD Value of Cotton Leaves under Verticillium Wilt Stress Based on GWO-ELM. *Agronomy* **2023**, *13*, 1779. [CrossRef]

46. Liu, T.; Xu, T.; Yu, F.; Yuan, Q.; Guo, Z.; Xu, B. A method combining ELM and PLSR (ELM-P) for estimating chlorophyll content in rice with feature bands extracted by an improved ant colony optimization algorithm. *Comput. Electron. Agric.* **2021**, *186*, 106177. [CrossRef]
47. Chu, F.; Wang, G.; Wang, J.; Chen, C.; Wang, X. Learning broad learning system with controllable sparsity through L regularization. *Appl. Soft. Comput.* **2023**, *136*, 110068. [CrossRef]
48. Liu, L.; Liu, T.; Chen, C.; Wang, Y. Modal-Regression-Based Broad Learning System for Robust Regression and Classification. *IEEE Trans. Neural Netw. Learn. Syst.* **2023**, *35*, 12344–12357. [CrossRef]
49. Wang, X.; Ling, B.; Zhao, H.; Liu, S. The Tensor Discriminant Ridge Regression Model With Extreme Learning Machine for Hyperspectral Image Classification. *IEEE J. Sel. Top. Appl. Earth Observ. Remote Sens.* **2023**, *16*, 8102–8114. [CrossRef]
50. Viskari, T.; Shiklomanov, A.; Dietze, M.C.; Serbin, S.P. The influence of canopy radiation parameter uncertainty on model projections of terrestrial carbon and energy cycling. *PLoS ONE* **2019**, *14*, e0216512. [CrossRef]
51. Hovi, A.; Janoutová, R.; Malenovský, Z.; Schraik, D.; Gastellu-Etchegorry, J.P.; Lauret, N.; Novotný, J.; Rautiainen, M. Physically based modelling of spectral transmittance through forest canopies. *Methods Ecol. Evol.* **2024**, *15*, 1859–1872. [CrossRef]
52. Ban, S.; Liu, W.; Tian, M.; Wang, Q.; Yuan, T.; Chang, Q.; Li, L. Rice Leaf Chlorophyll Content Estimation Using UAV-Based Spectral Images in Different Regions. *Agronomy* **2022**, *12*, 2832. [CrossRef]
53. He, J.; Zhang, N.; Su, X.; Lu, J.; Yao, X.; Cheng, T.; Zhu, Y.; Cao, W.; Tian, Y. Estimating Leaf Area Index with a New Vegetation Index Considering the Influence of Rice Panicles. *Remote Sens.* **2019**, *11*, 1809. [CrossRef]
54. Zhang, Y.; Jiang, Y.; Xu, B.; Yang, G.; Feng, H.; Yang, X.; Yang, H.; Liu, C.; Cheng, Z.; Feng, Z. Study on the Estimation of Leaf Area Index in Rice Based on UAV RGB and Multispectral Data. *Remote Sens.* **2024**, *16*, 3049. [CrossRef]
55. Yang, X.; Lu, X.; Shi, J.; Li, J.; Ju, W. Inversion of Rice Leaf Chlorophyll Content Based on Sentinel-2 Satellite Data. *Spectrosc. Spectr. Anal.* **2022**, *42*, 866–872. [CrossRef]